A primary microcephaly-associated *sas-6* mutation perturbs centrosome duplication, dendrite morphogenesis, and ciliogenesis in *Caenorhabditis elegans*

Mary Bergwell[1*], Amy Smith[2*], Ellie Smith[3§], Carter Dierlam[3§], Ramon Duran[3], Erin Haastrup[3], Rebekah Napier-Jameson[4], Rory Seidel[3], William Potter[3], Adam Norris[4], and Jyoti Iyer[3#]

* and § These authors contributed equally to this work

From [1]Oklahoma Medical Research Foundation, Oklahoma City, OK 73104, [2]Pfizer Inc., 875 Chesterfield Parkway West, Chesterfield, MO 63017, [3]Department of Chemistry and Biochemistry, University of Tulsa, Tulsa, OK 74104, [4]Southern Methodist University, PO Box 750100, Dallas, TX 75275

Running Head: *sas-6(L69T)* affects centrioles and cilia

[#]To whom correspondence should be addressed:

Jyoti Iyer: [3]Department of Chemistry and Biochemistry, University of Tulsa, Tulsa, OK 74104; jgi2708@utulsa.edu; Tel. (918) 631-2070.

Keywords: SAS-6, SASS6, rare disease, microcephaly, centrosome, centriole, cilia, *C. elegans*

Abstract

The human SASS6(I62T) missense mutation has been linked with the incidence of primary microcephaly in a Pakistani family, although the mechanisms by which this mutation causes disease remain unclear. The SASS6(I62T) mutation corresponds to SAS-6(L69T) in *C. elegans*. Given that SAS-6 is highly conserved, we modeled this mutation in *C. elegans* and examined *sas-6(L69T)* effect on centrosome duplication, ciliogenesis and dendrite morphogenesis. Our studies revealed that all the above processes are perturbed by the *sas-6(L69T)* mutation. Specifically, *C. elegans* carrying the *sas-6(L69T)* mutation exhibit an increased failure of centrosome duplication in a sensitized genetic background. Further, worms carrying this mutation also display shortened phasmid cilia, an abnormal phasmid cilia morphology, shorter phasmid dendrites and chemotaxis defects. Our data show that the centrosome duplication defects caused by this mutation are only uncovered in a sensitized genetic background, indicating that these defects are mild. However, the ciliogenesis and dendritic defects caused by this mutation are evident in an otherwise wild-type background, indicating that they are stronger defects. Thus, our studies shed light on the novel mechanisms by which the *sas-6(L69T)* mutation could contribute to the incidence of primary microcephaly in humans.

Introduction

Autosomal recessive primary microcephaly (MCPH) is a rare disease that causes a reduced brain size in infants along with a host of other physical and intellectual disabilities (Zaqout et al. 2017). According to the OMIM database, thirty microcephaly loci named MCPH1-MCPH30 have been identified thus far (https://www.omim.org/entry/251200). The current consensus in the field is that most mutations linked to the incidence of MCPH deplete the pool of neural progenitor cells during brain development. This results in fewer neurons being produced during embryonic development, thereby leading to a smaller brain size (Phan and Holland 2021). Although some MCPH-associated mutations have been previously modeled in *in vivo* model systems to

47 understand how MCPH-associated mutations contribute to the disease pathology, there are still
48 many MCPH-linked mutations that remain uninvestigated (Phan and Holland 2021). One such
49 MCPH-associated mutation is a mutation within the *SASS6* gene (*sas-6* in *C. elegans*) (Khan et
50 al. 2014). In 2014, a study by Khan et al. identified a leucine to threonine missense mutation in
51 the human *SASS6* gene to be associated with the incidence of MCPH in a consanguineous
52 Pakistani family (Khan et al. 2014).

53 SAS-6 protein function is conserved amongst several species including the multicellular
54 eukaryotic nematode *C. elegans* and humans (Dammermann et al. 2004, Leidel et al. 2005).
55 The *sas-6* gene was first identified to regulate centrosome duplication in *C. elegans*
56 (Dammermann et al. 2004, Leidel et al. 2005). Centrosomes consist of a pair of cylindrical
57 centrioles: a mother and a daughter centriole that are embedded in pericentriolar material. Major
58 functions of these organelles involve organizing a mitotic spindle and aiding in cilia assembly
59 (Nigg and Holland, 2018). Proper cell division requires a precise duplication of centrosomes.
60 There are two levels of regulation of centrosome duplication. First, it is critical that centrioles
61 duplicate only once per cell cycle, and second, it is imperative that each mother centriole gives
62 rise to a single daughter centriole. Defects in centrosome duplication can impair proper
63 chromosome segregation, leading to genome instability and aneuploidy. Indeed, increasing
64 centrosome numbers by elevating the expression levels of the master centrosome duplication
65 kinase Plk4 (ZYG-1 in *C. elegans*) is sufficient to induce tumorigenesis in mice (Levine et al.
66 2017). ZYG-1 and SAS-6 both play a critical role in mediating centrosome duplication
67 (O'Connell et al. 2001, Dammermann et al. 2004, Leidel et al. 2005). SAS-6 is recruited to the
68 mother centriole through its direct interaction with ZYG-1 and with another centriolar protein
69 SAS-5 (Lettman et al. 2013). These interactions are essential to initiate centriole assembly.

70 In addition to regulating centrosome biogenesis, SAS-6 function is also essential for cilia
71 assembly in *C. elegans* (Li et al. 2017). Cilia are microtubule-based organelles that are critical

72 for cell signaling and development (Drummond 2012). Sensory cilia are the sole type of cilia that
73 are present in *C. elegans.* These cilia are non-motile in nature and they play an essential role in
74 sensing the extracellular environment (Inglis et al. 2007). There are a total of sixty ciliated
75 sensory neurons in *C. elegans* hermaphrodites. The cilia are present at the dendritic ends of the
76 sensory neurons (Inglis et al. 2007). Although a previous study has shown that SAS-6 function
77 is critical for proper ciliogenesis (Li et al. 2017), the mechanism by which SAS-6 promotes
78 ciliogenesis is unknown. It has been especially difficult to study the role of SAS-6 in ciliogenesis
79 because *sas-6/SASS6* is an essential gene (Kamath et al. 2003, Blomen et al. 2015). Due to the
80 important role of SAS-6 in regulating centrosome duplication, most mutations in *sas-6* yield
81 embryonic lethality or sterility (Dammermann et al. 2004, Leidel et al. 2005, O'Rourke et al.
82 2011, Song et al. 2011, The C. elegans Deletion Mutant Consortium et al. 2012, Lettman et al.
83 2013).

84 Ciliogenesis defects have been proposed as an important underlying cause of
85 microcephaly (Alcantara et al. 2014, Gabriel et al. 2016, Broix et al. 2018, Wambach et al. 2018,
86 Zhang et al. 2019, Ding et al. 2019, Sohayeb et al. 2020, Farooq et al. 2020). However, the
87 effect of this *SASS6* mutation on ciliogenesis has never been investigated. The effect of the
88 MCPH-associated *SASS6* mutation on centrosome duplication in its endogenous context has
89 also not been determined thus far. It is important to note that SASS6 levels in the cell are tightly
90 regulated. An increase or a decrease in SASS6/SAS-6 levels causes either centrosome
91 overduplication or a failure of centrosome duplication, respectively (Dammermann et al. 2004,
92 Leidel et al. 2005). Therefore, it is critical to model the MCPH-associated *SASS6* mutation in an
93 endogenous context in a multicellular eukaryotic animal model. However, to date such a study
94 has not been reported.

95 In this study, we used CRISPR/Cas9 genome editing to re-create the MCPH-associated
96 *sas-6(L69T)* mutation in *C. elegans*. Our *in vivo* studies in the worm indicate that the *sas-*

97 *6(L69T)* mutation does not result in embryonic lethality when this is the sole mutation in *sas-6* in
98 an otherwise wild-type background. However, introducing this mutation into a tight temperature-
99 sensitive *zyg-1(it25)* strain that is partially compromised for centrosome duplication results in a
100 robust increase in embryonic lethality at the semi-permissive temperature. These data indicate
101 that this MCPH-associated mutation mildly perturbs centrosome duplication in *C. elegans.*
102 Surprisingly, while the centrosome duplication defects were only observed in a sensitized
103 genetic background, ciliogenesis and dendritic defects were observed even in a wild-type
104 background in *C. elegans* carrying the *sas-6(L69T)* mutation. Specifically, our studies reveal
105 that the *sas-6(L69T)* mutation causes a reduction of the phasmid cilia and phasmid dendrite
106 lengths and results in an abnormal phasmid cilia morphology. Thus, our studies indicate that the
107 MCPH-associated *sas-6(L69T)* mutation affects ciliogenesis and dendrite morphogenesis more
108 severely than centrosome duplication in *C. elegans.* In conclusion, our studies have uncovered
109 a novel role of the MCPH-associated *sas-6(L69T)* mutation in regulating ciliogenesis and
110 dendrite morphogenesis in the worm.

111 **Materials and Methods**

112 ***C. elegans* maintenance**

113 All *C. elegans* strains were grown at 20°C on OP50 *E. coli* bacteria seeded onto MYOB agar
114 plates, unless otherwise indicated (as in the case of different assays). **Table S1** lists all the *C.*
115 *elegans* strains that have been generated and used in this study.

116 **CRISPR/Cas9 genome editing**

117 Assembled ribonucleoprotein complexes were microinjected into *C. elegans* gonads to perform
118 CRISPR/Cas9 genome editing as described previously (Paix et al. 2015, Paix et al. 2016, Iyer et
119 al. 2019, Smith et al. 2020). Homozygosity of the *sas-6(L69T)* edit was confirmed by PCR
120 followed by restriction digestion with EcoRI and by DNA sequencing. Note that the EcoRI

121 restriction site was introduced by silent mutagenesis of the *sas-6* gene sequence. Therefore, it
122 is not expected to alter the final sequence of the SAS-6 protein. **Table S2** lists the sequences of
123 the screening primers, guide RNAs and repair templates that were used to make the CRISPR
124 strains that have been used in this study.

125 **Brood count and embryonic viability assays**

126 All brood count assays and embryonic viability assays were performed as described previously
127 (Xie et al. 2022). For both brood count as well as embryonic viability assays, L4 stage *C.*
128 *elegans* were plated at the respective indicated temperatures. For brood count assays, all the
129 progeny that were produced by each single worm over the worm's reproductive lifespan were
130 counted and quantified. For embryonic viability assays, the percentage of dead and live progeny
131 produced by each worm was determined by counting. The percentage of viable progeny was
132 then computed by dividing the number of live progeny by the total number of progeny and by
133 multiplying this ratio by 100.

134 **Confocal live imaging of centrosome duplication**

135 To monitor centrosome duplication in *C. elegans* embryos, live imaging was performed using an
136 Olympus Spinning-Disk confocal microscope mounted with a Yokagawa scanhead. The
137 cellSens software (Olympus America Inc., Waltham, MA) was used for image acquisition and
138 processing. To prepare the *C. elegans* strains for imaging, L4 stage *C. elegans* were plated at
139 21.8°C overnight. The next day, gravid adult worms were picked into 8 to 12 µl of egg buffer
140 (118 mM NaCl, 47 mM KCl, 2 mM $CaCl_2$, 2 mM $MgCl_2$, 5 mM HEPES pH 7.4) on a square glass
141 coverslip and dissected near the vulva using a needle to release embryos. The coverslip was
142 carefully mounted on a 2% agarose pad (2% agarose LE in M9 buffer). The edges of the
143 coverslip were sealed with molten Vaseline using a paintbrush. These slides were subjected to
144 time-lapse imaging by taking 1.25 µm Z-stacks over an interval of approximately 132 seconds.

145 Maximum intensity Z-projections were computed using the cellSens software (Olympus America
146 Inc.) and converted into an AVI format for making videos. The brightness and contrast were
147 adjusted for the control and *sas-6(L69T)* videos for better non-quantitative video visualization.

148 **Genetic crosses**

149 To introduce the *sas-6(L69T)* mutation into the *zyg-1(it25)* background, first, males were
150 generated from the *zyg-1(it25)* strain using alcohol treatment. Specifically, L4 stage
151 hermaphrodites from the *zyg-1(it25)* strain were incubated with 10% ethanol in M9 buffer for 30
152 minutes, washed thrice with M9 buffer and allowed to recover for an hour. After recovery, the
153 worms were plated onto MYOB plates and incubated at 20°C until males appeared. Following
154 this, *zyg-1(it25)* homozygous males were mated with *sas-6(L69T)* L4 hermaphrodites. The F1
155 progeny from this cross were screened for heterozygosity of the *sas-6(L69T)* mutation using
156 PCR and restriction digestion. Cross progeny were identified and screened for homozygosity of
157 both edits using PCR and restriction digestion (for homozygosity screening of the *sas-6(L69T)*
158 mutation) and 24°C temperature shifts (for homozygosity screening of the *zyg-1(it25)* mutation).
159 Homozygosity of fluorescent markers was confirmed by confocal fluorescence imaging.
160 For the cilia imaging experiments, PY6100 males *(oyIs59[osm-6p::gfp] III)* were crossed with
161 hermaphrodites from the IYR001 (*sas-6(luv1[sas-6::ha]) IV*) and IYR002 (*sas-6(luv2[sas-*
162 *6[L69T])) IV*) strains to produce strains expressing either SAS-6::HA (control) or SAS-
163 6(L69T)::HA along with a pan-ciliary GFP marker. These strains were named IYR026 and
164 IYR027, respectively. F1 progeny were screened for heterozygosity at both loci by screening F1
165 hermaphrodites for the presence of GFP fluorescence in the phasmid neurons. F2 homozygotes
166 for *sas-6::ha* were identified as described previously (Bergwell et al. 2019) by PCR and
167 digestion by NdeI followed by agarose gel electrophoresis. F2 homozygotes for *sas-6(L69T)::ha*
168 were identified by PCR and digestion by EcoRI followed by agarose gel electrophoresis.

169 **Modeling SAS-6(L69T) using AlphaFold2**

170 The N-terminal coiled-coil dimer construct of *C. elegans* centriolar protein SAS-6 was
171 crystallized by Hilbert et al. 2013. The ceSAS-constructs required for crystallization involved the
172 removal of the α2-β5 loop (Δ103-130) which was reported to not affect the N-terminal domain
173 structure within a C_α rmsds of ~0.3 Angstroms. The crystallographic data was deposited in the
174 Research Collaboration for Structural Bioinformatics databank under accession number PDB ID
175 code 4G79.

176 The native SAS-6 structure (AF-062479-F1) available from the AlphaFold Protein
177 Structure Database (Jumper et al. 2021; https://AlphaFold.ebi.ac.uk/) has leucine at position 69
178 at the end of the β_4 sheet just prior to the asparagine-asparagine which initiates the α_1 helix
179 occurring at positions 70 to 82 (using the Hilbert et al. 2013 author numbering system). It
180 should be noted that the residue numbering system reported for ceSAS-6 in Uniprot (062479)
181 has two additional amino acids (glycine-serine) at the N-terminus and thus the sequence is
182 offset and the α_1 helix starts at position 72 in this numbering system. The reported per-residue
183 confidence score (pLDDT) for residue leucine 69 was 92.37 suggesting that the AlphaFold
184 model confidence level was very high for this residue.

185 The SAS-6(L69T) mutant protein structure containing the single leucine to threonine
186 substitution was modeled by loading the modified sequence into the Google Colaboratory
187 (Colab) services using ColabFold: AlphaFold2 using MMseqs2 as described by Mirdita et al.
188 2022, and available through the AlphaFold2.ipynb v2.1.0. with the suite of public notebooks
189 available through the deepmind/AlphaFold github. The 4G79 and the AlphaFold models were
190 uploaded into the program ChimeraX (https://www.cgl.ucsf.edu/chimerax/) developed from the
191 Resource for Biocomputing, Visualization, and Informatics for Visualization (RBVI), University of
192 California, San Francisco.

193 The Molecular Lipophilicity Potential (MLP) is a construct that spreads atomic values out
194 in 3D. The MLP coloring on the molecular surface is based on pyMLP

195 (https://www.rbvi.ucsf.edu/chimerax/docs/user/commands/mlp.html) as originally developed by
196 Broto et al. 1984 and Laguerre et al. 1997 and as modified
197 https://www.cgl.ucsf.edu/chimera/data/mlp-sep2016/index.html and was used without any color
198 scale modifications.

199 **_C. elegans_ phasmid cilia and dendrite imaging**

200 *C. elegans* phasmid cilia and dendrites were imaged as described previously (Xie et al. 2022).
201 For the phasmid and dendrite imaging experiments, a new strain IYR040 (*oyIs59 [osm-6p::gfp]*
202 *III; sas-6(luv40)*) *IV*) was created by CRISPR/Cas9 editing of the IYR026 strain. Specifically, to
203 generate the IYR040 strain, the IYR026 strain (*oyIs59 [osm-6p::gfp] III; sas-6(luv1[sas-6::ha])*
204 *IV*) was CRISPR-edited using the same guide RNA and the repair template that was used to
205 introduce the leucine 69 to threonine (L69T) mutation, with the only exception that the IYR040
206 repair template lacked the L69T mutation. As a result, the IYR040 strain is genetically identical
207 to the IYR027 strain except that it is wild-type for SAS-6. This strain served as a control for all of
208 our phasmid cilia and dendrite imaging experiments. For the phasmid cilia and dendrite imaging
209 assays, L4 stage *C. elegans* from the IYR040 and IYR027 strains were grown at 16°C
210 overnight. The next day, young adult worms were anaesthetized using 10 mM Levamisole,
211 mounted on 2% agarose pads and imaged within 30 minutes using an Olympus IX83 Spinning
212 Disk confocal microscope coupled with a Yokogawa X1 Scan head (Olympus America Inc.).
213 0.25 µm Z-slices were taken from the top to the bottom of each phasmid neuron using the
214 cellSens software (Olympus America Inc.). All images were taken at the same laser intensity
215 and exposure time.

216 **Phasmid cilia and dendrite length quantification**

217 To quantify phasmid cilia and dendrite lengths, the raw .vsi files that were captured using the
218 cellSens software (Olympus America Inc.) were opened in ImageJ using the OlympusImageJ
219 Plugin. ImageJ (Abràmoff et al. 2004) was then used to convert the raw data into maximum
220 intensity Z-projections. The scale was set to 1 pixel = 110 nm. Since the expression of GFP in

221 the phasmid neurons varied from worm to worm, the brightness and contrast were adjusted
222 non-uniformly to delineate the beginning and end of each phasmid cilium to ensure an accurate
223 measurement of the phasmid cilia lengths. For the dendrite imaging, the single frame view was
224 used in cellSens (Olympus America, Inc.) to visualize the beginning and end of each phasmid
225 dendrite in 3D to ensure that the dendrite lengths were being properly measured. Dendrites and
226 cilia whose beginning or end could not be delineated were excluded from our analysis. To
227 measure cilia and dendrite lengths, a line was traced along the entire length of the cilium or the
228 dendrite using the Segmented Lines tool in ImageJ (Abràmoff et al. 2004). The lengths of the
229 shorter of the two phasmid dendrites and the longer of the two phasmid cilia were then
230 measured in micrometers using ImageJ (Abràmoff et al. 2004) and have been presented in
231 **Figures 5D** and **7C**.

232 **Criteria used for quantifying phasmid cilia morphology defects**

233 Phasmid cilia that did not exhibit the canonical phasmid cilia structure with two transition zones
234 and cilia projecting from the transition zones were quantified as having an abnormal phasmid
235 cilia morphology. Specifically, instances where the transition zones could not be clearly
236 distinguished from the ciliary axoneme or where we were unable to clearly identify the transition
237 zone due to additional transition zone-like GFP aggregates being present in the vicinity of the
238 transition zone were classified as being abnormal.

239 ***C. elegans* chemotaxis assay**

240 Olfaction assays were performed as previously described in Liang et al. 2022.
241 Briefly, *C. elegans* were maintained by standard techniques on NGM agar plates seeded with
242 OP50 *Escherichia coli* at 20˚C. Worms were synchronized to L4 stage. Worms were washed off
243 the plates using M9 buffer, allowed to gravity settle, supernatant removed, and then washed a
244 further 4 times. Unseeded NGM plates (50 mM NaCl, 1.7% agar, 0.25% peptone, 1 mM $CaCl_2$,
245 0.013 mM Cholesterol, 1 mM $MgSO_4$, 25 mM KPO_4) were divided into four quadrants, two with
246 solvent and two with odorant. Ethanol was used as a solvent. A 1:500 dilution of the odorant

247 butanone was made in ethanol. The Chemotaxis Index (CI) was calculated using the formula CI
248 = (# animals in two odorant quadrants)/(# animals in any of the four quadrants). Four plates
249 were used per genotype per experiment. Assays were repeated 3 times. For each of the three
250 independent trials, 569, 704 and 1552 control (*sas-6::ha*) worms respectively, and 522, 526 and
251 663 *sas-6(L69T)* worms respectively, were analyzed for their chemotaxis towards 1:500
252 butanone.

253 **Whole worm extracts for western blotting**

254 Whole worm extracts for western blotting were prepared as described previously (Xie et al.
255 2022). Briefly, 100 gravid adults from each genotype were washed with M9 buffer twice. The M9
256 buffer was removed and the worm pellet was resuspended in 40 µl of 4X SDS PAGE sample
257 buffer, boiled for 10 minutes at 95°C and stored at -30°C until further use.

258 **Western blotting**

259 Western blotting was performed using the Bio-Rad wet-transfer method as described previously
260 (Xie et al. 2022). Briefly, for western blotting of whole worm extracts, 10 to 14 µl of extracts were
261 loaded onto each well of a 7.5% SDS-PAGE gel. The gels were run until proper band separation
262 was achieved and the protein was transferred onto a 0.2 µm nitrocellulose membrane using the
263 wet-transfer method (Bio-Rad Laboratories). The membranes were blocked with Odyssey
264 Blocking Buffer (LiCOR Biosciences, Inc.), probed with anti-HA (Cell Signaling, catalog C29F4
265 Rabbit mAb #3724) and anti-tubulin (Santa Cruz Biotechnology, Inc., catalog sc-32293)
266 antibodies overnight at 4°C. The membranes were washed thrice with 1X TBST (0.1% w/v
267 Tween-20, 50 mM Tris-Cl, pH 7.6, 150 mM NaCl) and incubated with IRDye® 800CW Donkey
268 anti-Rabbit IgG secondary antibody (LiCOR Biosciences, Inc. catalog # 926-32213) and IRDye®
269 680RD Goat anti-Mouse IgG secondary antibody (LiCOR Biosciences, Inc. catalog # 926-
270 68070) for 1 hour at room temperature. The membranes were washed again thrice with
271 1XTBST and imaged using the LI-COR Odyssey CLx imager (LI-COR Biosciences, Inc.). The

272 band intensities were adjusted equally for all the gel lanes for better data visualization and
273 presentation. **Table S3** lists all the antibodies that have been used in this study.

274 **Western blot quantification and image presentation**

275 The band intensities across the entire membrane were uniformly adjusted using the LiCOR
276 Image Studio software (LI-COR Biosciences, Inc.) and saved in a .tiff format for performing
277 quantitative analysis of the bands. Quantitative western blotting was performed using ImageJ
278 (Abràmoff et al. 2004). Briefly, the band intensities for SAS-6::HA were determined using
279 ImageJ and normalized with respect to the loading control Tubulin. ImageJ was also used to
280 rotate and crop representative gel images presented in **Figure S1** and in all other fluorescence
281 images that are presented in this paper**.** For all images, scale bars from the original images
282 were cropped and grouped with their corresponding original images.

283 **Statistical analysis**

284 Graphpad Prism (GraphPad Software, Inc.) was used for performing statistical analysis of the
285 data. Unpaired two-tailed t-tests were performed to determine statistical significance of the data
286 for the brood counts, western blot assays, phasmid cilia lengths, phasmid dendrite lengths and
287 chemotaxis assays. The Fisher's exact test was performed to determine if the phasmid cilia
288 morphology defects were statistically significant. A p-value of less than 0.05 was considered to
289 attain statistical significance.

290 **Results**

291 An isoleucine to threonine substitution of SASS6 was reported to be linked with the occurrence
292 of MCPH in a Pakistani family (Khan et al. 2014). As shown previously by Khan et al., alignment
293 of the amino acid sequences of the SAS-6 protein of different species showed that the MCPH-
294 associated amino acid of human SASS6 is remarkably conserved among several species
295 including *C. elegans* (Khan et al. 2014). Notably, the *sas-6* gene was first identified in *C.*
296 *elegans* and was subsequently shown to function similarly in humans (Dammermann et al.

297 2004, Leidel et al. 2005). Due to the high functional conservation of SAS-6, we determined that
298 *C. elegans* would be an appropriate eukaryotic model to thoroughly investigate the
299 consequences of this mutation. The human SASS6(I62T) mutation corresponds to SAS-6(L69T)
300 in *C. elegans.*

301 **The *sas-6(L69T)* mutation was successfully introduced into *C. elegans* by CRISPR/Cas9**
302 **editing**

303 Using CRISPR/Cas9 genome editing, we generated a leucine to threonine substitution at
304 amino acid 69 of the *C. elegans* SAS-6 protein by editing the endogenous *sas-6* gene of *C.*
305 *elegans.* This strain was named IYR002 and the corresponding allele was named *sas-6(luv2).*
306 For ease of understanding, this strain has been referred to as the *sas-6(L69T)* strain and the
307 corresponding MCPH-associated mutation has been referred to as the *sas-6(L69T)* mutation
308 throughout this manuscript. The repair template used for introducing the *sas-6(L69T)* mutation
309 carried an EcoRI restriction site **(Figure 1A)**. As shown in **Figure 1B**, upon PCR amplification
310 and restriction digestion of the *sas-6* gene with EcoRI, several homozygous edited worms were
311 obtained in the F2 generation (lanes with black stars). The incorporation of the *sas-6(L69T)*
312 mutation was also confirmed by DNA sequencing.

313 **The microcephaly-associated *sas-6(L69T)* mutation does not affect brood size or**
314 **embryonic viability in a wild-type background**

315 The function of the *sas-6* gene is essential for centrosome duplication (Dammermann et
316 al. 2004, Leidel et al. 2005). Proper centrosome duplication is required for accurate embryonic
317 divisions in *C. elegans.* Since the *sas-6(L69T)* mutation has a pathological relevance in
318 humans, we proposed that this mutation could impair SAS-6 function in regulating centrosome
319 duplication, thereby leading to defective centrosome duplication in *C. elegans*. This could, in
320 turn, affect *C. elegans* brood size and embryonic viability. Therefore, to investigate the effect of

321 the *sas-6(L69T)* mutation on centrosome duplication, brood counts and embryonic viability
322 assays were performed using *C. elegans* carrying this mutation. Surprisingly, the introduction of
323 the *sas-6(L69T)* mutation did not yield any major effect on either brood size or embryonic
324 viability at 16˚C, 20˚C and 25˚C as compared with control worms (wild-type N2 worms with HA-
325 tagged endogenous *sas-6*) **(Figures 2A and 2B)**. These data indicate that the *sas-6(L69T)*
326 mutation does not severely perturb SAS-6 function in regulating centrosome duplication.

327 **The *sas-6(L69T)* mutation increases centrosome duplication failures and embryonic**
328 **lethality in a sensitized *zyg-1(it25)* background**

329 ZYG-1 is a functional homolog of human Plk4 and a master kinase whose activity is
330 critical for proper centrosome duplication (O'Connell et al. 2001, Habedanck et al. 2005,
331 Bettencourt-Dias et al. 2005). Decreasing ZYG-1 protein levels causes a failure of centrosome
332 duplication while elevating them causes centrosome overduplication (O'Connell et al. 2001,
333 Peel et al. 2017, Wolf et al. 2018). The temperature-sensitive *zyg-1(it25)* allele has a proline to
334 leucine substitution within the ZYG-1 cryptic polo box which impairs ZYG-1 function at the
335 restrictive temperature, leading to a failure of proper centrosome duplication (Kemphues et al.
336 1988, Kemp et al. 2007). By controlling the temperature at which the *zyg-1(it25)* strain is grown,
337 the rate of centrosome duplication failure in this strain can be controlled. For example, at a
338 restrictive temperature of 24°C and above, the *zyg-1(it25)* strain produces 100% dead embryos
339 due to a complete failure of centrosome duplication (Kemp et al. 2007). However, at lower semi-
340 permissive temperatures (temperatures below 24°C), centrosome duplication still partially
341 occurs in the *zyg-1(it25)* strain, yielding varying levels of embryonic viability with a temperature
342 of 20°C yielding between 93.7% to 98.7% embryonic viability (Song et al. 2008). ZYG-1 directly
343 interacts with SAS-6 (Lettman et al. 2013) and functions upstream of SAS-6 in the centrosome
344 duplication pathway (Leidel et al. 2005, Delattre et al. 2006, Pelletier et al. 2006). Therefore, we
345 questioned whether we could use the *zyg-1(it25)* allele to uncover any potential mild defects in

346 SAS-6 function in regulating centrosome duplication that could be present in the *sas-6(L69T)*
347 mutants. To address this, we first obtained a *zyg-1(it25)* strain expressing fluorescently-tagged
348 centrosome (mCherry::SPD-2) and chromosome (GFP::histone) markers (OC869 from the
349 O'Connell lab) to visualize centrosome duplication. This strain served as a control for our
350 experiment and has been referred to as the *zyg-1(it25)* strain in **Figure 3**. Using this strain as
351 the background strain, as shown in **Figure 3A,** we performed genetic crossing to combine the
352 *sas-6(L69T)* and *zyg-1(it25)* mutations. This strain has been referred to as the *zyg-1(it25);sas-*
353 *6(L69T)* strain in **Figure 3.** We reasoned that if the *sas-6(L69T)* mutation mildly affects SAS-6
354 function in regulating centrosome duplication, combining it with the *zyg-1(it25)* mutation at the
355 semi-permissive temperature would yield higher levels of centrosome duplication failures and
356 increased embryonic lethality than what each mutant produces on its own.

357 Upon introducing the *sas-6(L69T)* mutation into the *zyg-1(it25)* strain expressing
358 fluorescent centrosome and chromosome markers, centrosome duplication in the *zyg-1(it25)*
359 and *zyg-1(it25);sas-6(L69T)* worms was assessed at the semi-permissive temperature of 21.8°C
360 **(Figures 3B and 3C)**. Notably, introducing the *sas-6(L69T)* mutation greatly increased the
361 centrosome duplication failures exhibited by the *zyg-1(it25)* mutants at 21.8°C **(Figure 3C)**.
362 Specifically, in the *zyg-1(it25)* single mutant alone, about 83% of the centrosomes analyzed
363 duplicated normally at the semi-permissive temperature of 21.8°C (n=52). However,
364 interestingly, in the *zyg-1(it25);sas-6(L69T)* double mutant, proper centrosome duplication was
365 reduced to only about 28% (n=58). Since accurate centrosome duplication is required for
366 embryonic viability, we next assessed whether embryonic viability of the *zyg-1(it25)* strain was
367 also affected in the presence of the *sas-6(L69T)* mutation.

368 The embryonic viability of the *zyg-1(it25)* strain expressing fluorescent markers alone at
369 the semi-permissive temperature of 21.7°C was about 44% (number of worms=18; number of
370 progeny= 1103). However, introducing the *sas-6(L69T)* mutation into this background reduced

371 embryonic viability to only about 7% (number of worms=18; number of progeny= 912; unpaired
372 two-tailed t-test p<0.0001) **(Figure 3D)**. These data collectively indicate that the *sas-6(L69T)*
373 mutation mildly inhibits SAS-6 function in regulating centrosome duplication, thereby resulting in
374 a failure of proper centrosome duplication and increased embryonic lethality in the *zyg-1(it25)*
375 background.

376 **Modeling SAS-6(L69T) using AlphaFold2 suggests that the leucine to threonine**
377 **substitution at amino acid 69 does not have a major effect on SAS-6 protein structure**

378 The L69T mutation is located within the conserved PISA (Present In SAS-6) motif of
379 SAS-6 **(Figure 4A)**. Further, this amino acid does not have a known involvement in the
380 dimerization of SAS-6 coiled-coil region, in the interaction of SAS-6 N-terminal head domains, in
381 the interaction of SAS-6 with ZYG-1 or in the interaction of SAS-6 with SAS-5 (van Breugel et al.
382 2011, Kitagawa et al. 2011, Qiao et al. 2013, Hilbert et al. 2013, Lettman et al. 2013, Busch et
383 al. 2019) **(Figure 4A)**. To elucidate the possible mechanism by which the *sas-6(L69T)* mutation
384 affects centrosome duplication, we used AlphaFold2 to predict how the L69T mutation could
385 alter the structure of the SAS-6 protein **(Figures 4B, 4C)**. **Figures 4B and 4C** show the
386 comparison of the SAS-6 PDB model 4G79 from Hilbert et al. 2013 **(Figure 4B)** compared with
387 the AlphaFold2-derived SAS-6(L69T) model **(Figure 4C)** using the ChimeraX program. Our
388 analysis indicates that the overall structural differences due to the L69T mutation in SAS-6 are
389 minor. Therefore, we propose that centriole architecture may not be significantly affected in the
390 *sas-6(L69T)* mutant worms. This is supported by our data that *C. elegans* carrying homozygous
391 copies of the *sas-6(L69T)* mutation are close to 100% viable at all temperatures **(Figure 2B)**.
392 However, the ChimeraX hydrophobicity surface model suggests that a deep hydrophobic pocket
393 that is found within the SAS-6 protein is reduced due to the MCPH-associated L69T mutation
394 **(Figures 4B, 4C, dark blue arrows)**. The function of this hydrophobic pocket within SAS-6 has
395 not yet been elucidated.

396 **SAS-6 protein levels are altered in the presence of the *sas-6(L69T)* mutation in a *zyg-***
397 ***1(it25)* background but not in a wild-type background**

398 Some of the other known MCPH-associated mutations in centrosome duplication genes
399 such as STIL and PLK4 have been reported to affect their protein levels (Patwardhan et al.
400 2018, Martin et al. 2014). The effect of *sas-6(L69T)* mutation on SAS-6 protein levels is
401 unknown. Therefore, we questioned whether the *sas-6(L69T)* mutation has any effect on SAS-6
402 protein levels. To address this, western blotting was performed on whole worm lysates from
403 *zyg-1(it25);sas-6::ha* (control) vs *zyg-1(it25);sas-6(L69T)::ha* worms and from *sas-6::ha* (control)
404 vs *sas-6(L69T)::ha* worms. Western blot analysis indicated that SAS-6 levels decrease on
405 average by 15% in the presence of the *sas-6(L69T)* mutation in the *zyg-1(it25)* background
406 (n=4; p=0.0475, unpaired two-tailed t-test) **(Figure S1A, S1B)**. However, the decrease in SAS-6
407 protein levels in the presence of the *sas-6(L69T)* mutation in an otherwise wild-type background
408 was not found to be statistically significant (n=4; p=0.1398, unpaired two-tailed t-test) **(Figures**
409 **S1C, S1D)**.

410 **Ciliogenesis is perturbed in *sas-6(L69T)* mutant *C. elegans***

411 Ciliogenesis defects have been linked with the incidence of microcephaly (Alcantara et
412 al. 2014, Gabriel et al. 2016, Broix et al. 2018, Wambach et al. 2018, Zhang et al. 2019, Ding et
413 al. 2019, Sohayeb et al. 2020, Farooq et al. 2020). Defective ciliogenesis is thought to result in
414 cell cycle arrest in neural progenitors during brain development. The loss of neural progenitors
415 due to either cell-cycle arrest or apoptosis has been proposed to be an underlying cause for the
416 incidence of MCPH (Phan and Holland 2021). The effect of the *sas-6(L69T)* mutation on
417 ciliogenesis is currently unknown. Since ciliogenesis defects have been previously linked with
418 MCPH, we questioned whether worms carrying the *sas-6(L69T)* mutation exhibit any
419 ciliogenesis defects. Preliminary dye-filling assays (performed according to the protocol by
420 Power et al. 2020) did not reveal any severe dye-filling defects between control (wild-type N2

421 worms with HA-tagged endogenous SAS-6) and *sas-6(L69T)* worms. Specifically, we did not
422 observe any worm that completely excluded DiI in their phasmid neurons in either control or
423 *sas-6(L69T)* worms upon dye-filling. Our preliminary experiments revealed that 100% of the
424 control (n=23) and *sas-6(L69T)* (n=25) worms exhibited dye-filling with DiI. Nevertheless,
425 although dye-filling assays are a quick and easy method to visualize cilia defects, a lack of a
426 dye-filling defect phenotype does not exclude the presence of ciliary defects.

427 To directly determine whether the *sas-6(L69T)* strain exhibits ciliary defects, we obtained
428 a PY6100 strain that expresses a pan-ciliary marker. This strain expresses a GFP
429 transcriptional reporter for OSM-6*,* a protein that is critical for proper ciliogenesis (Perkins et al.
430 1986, Collet et al. 1998). Thus, the introduction of *osm-6p::GFP* marks *C. elegans* ciliated
431 sensory neurons with soluble GFP driven from the *osm-6* promoter, allowing for easy
432 visualization of the cilia (Bayer et al. 2020, Xie et al. 2022).

433 We introduced the *sas-6(L69T)* mutation into the PY6100 strain (*oyIs59 [osm-6p::gfp] III*)
434 by genetic crossing. The resultant strain was named IYR027. The experimental design for
435 combining *osm-6p::GFP* with the *sas-6(L69T)* mutation is shown in **Figure 5A.** The introduction
436 of *osm-6p::GFP* into the *sas-6(L69T)* strain by genetic crossing was confirmed by both confocal
437 microscopy and by genotyping using PCR. For ease of understanding, this new IYR027 strain
438 has been referred to as the *osm-6p::GFP;sas-6(L69T)* strain throughout the paper and has been
439 used to examine the cilia and dendritic defects that arise as a consequence of the *sas-6(L69T)*
440 mutation in **Figures 5, 6 and 7**.

441 Since the *sas-6(L69T)* strain also has an HA tag on the mutant SAS-6 protein, to create
442 an appropriate control strain, we first crossed the PY6100 strain with a strain expressing SAS-
443 6::HA to account for the potential effect of the HA-tag on SAS-6 function in regulating
444 ciliogenesis. This strain was named IYR026. We then CRISPR-edited the IYR026 strain to
445 make it genetically identical to the *osm-6p::GFP;sas-6(L69T)* strain except for the fact that this

446 new strain lacked the leucine 69 to threonine mutation. For convenience, we refer to this control
447 strain (IYR040) as the *osm-6p::GFP* strain. This strain served as the control for all the cilia and
448 dendrite analysis conducted in **Figures 5, 6 and 7**.

449 To investigate whether *sas-6(L69T)* mutant worms exhibit defects in ciliogenesis, we
450 examined the cilia of the phasmid neurons which are present in the posterior region of the
451 worms **(Figure 5B)**. Intriguingly, upon measuring the length of the phasmid neuronal cilia, we
452 found a significant decrease in the average ciliary length in the *osm-6p::GFP;sas-6(L69T)*
453 mutant worms **(Figure 5C, bottom panel, white bracket)** as compared with control (*osm-*
454 *6p::GFP)* worms **(Figure 5C, top panel, white bracket)**. Specifically, control *osm-6p::GFP*
455 worms had an average phasmid cilia length of about 5.82 μm (n=54) while the *osm-6p::GFP;*
456 *sas-6(L69T)* worms had shorter cilia with an average phasmid cilia length of only 3.99 μm
457 (n=59) (unpaired two-tailed t-test, $p<0.0001$). These data indicate that the *sas-6(L69T)* mutation
458 indeed perturbs ciliogenesis in *C. elegans.*

459 **Phasmid cilia morphology and dendrite length are defective in the *sas-6(L69T)* mutant**
460 **worms**

461 While analyzing cilia length of *osm-6p::GFP;sas-6(L69T)* worms, we found that some of
462 the cilia from this strain exhibited a disfigured cilia morphology as compared with control worms.
463 Our analysis revealed that 100% of the phasmid cilia of control (*osm-6p::gfp)* worms (n=61)
464 showed a normal phasmid cilia morphology with two distinct transition zones and a ciliary
465 axoneme projecting from each transition zone **(Figure 6A, 6B, 6D)**. However, 10 out of 65
466 (15.4%) of the *osm-6p::GFP;sas-6(L69T)* phasmid cilia exhibited an abnormal morphology
467 **(Figures 6A, 6C, 6D).** This abnormal phasmid cilia morphology defect of the *osm-6p::GFP; sas-*
468 *6(L69T)* worms was found to be statistically significant via a Fisher's exact test ($p=0.0014$).
469 These data indicate that the *sas-6(L69T)* mutation perturbs phasmid cilia morphology in a
470 subset of the phasmid cilia.

471 In addition to the phasmid cilia morphology defect, the *osm-6p::GFP;sas-6(L69T)* worms
472 also displayed a dendritic extension defect. In general, the average lengths of the phasmid
473 dendrites of control *osm-6p::GFP* worms **(Figure 7A)** were longer than those of *osm-*
474 *6p::GFP*;*sas-6(L69T)* worms **(Figure 7B)** . Specifically, phasmid dendrites analyzed from
475 control worms exhibited an average length of 37.4 μm (n=38). In contrast, the average length of
476 phasmid dendrites of *sas-6(L69T)* worms was 28.1 μm (n=42) **(Figure 7C).** This phasmid
477 dendrite length defect of the *osm-6p::GFP;sas-6(L69T)* worms was found to be statistically
478 significant via an unpaired two-tailed t-test ($p<0.0001$).

479 **Chemotaxis is defective in the *sas-6(L69T)* mutant worms**

480 Since defects in ciliogenesis in the *C. elegans* sensory neurons often affect worm
481 behaviors, we investigated the effect of the *sas-6(L69T)* mutation on chemotaxis to the
482 chemoattractant butanone. The experimental scheme for the chemotaxis assays is shown in
483 **Figure 8A**. Our studies demonstrated that *C. elegans* carrying the *sas-6(L69T)* mutation
484 exhibited a reduced attraction to 1:500 butanone as compared with control worms (two-tailed
485 unpaired t-test, $p<0.0001$) **(Figures 8B, 8C)**. Specifically, our data showed that the average
486 chemotaxis index of control worms (*sas-6::ha*) was 0.4107 (n=2825). In comparison, the
487 average chemotaxis index of *sas-6(L69T)* worms was reduced to 0.3307 (n=1711) **(Figures 8B,**
488 **8C)**. These data indicate that defective ciliogenesis in the *sas-6(L69T)* mutant worms likely
489 causes a defective *C. elegans* chemotaxis response to 1:500 butanone. Hence, SAS-6 function
490 in regulating ciliogenesis is likely to be important for mediating certain worm behaviors such as
491 chemotaxis.

492 Interestingly, chemotaxis towards butanone is predominantly controlled by the AWC
493 amphid sensory neurons (Bargmann et al. 1993). These data indicate that ciliogenesis may also
494 be perturbed in the amphid sensory neurons in *sas-6(L69T)* mutant worms. In the present study,
495 we have mainly focused our efforts on analyzing ciliogenesis in the *C. elegans* phasmid

496 neurons. Future studies should be directed towards determining whether ciliogenesis in the
497 amphid neurons is also affected in *C. elegans* carrying the *sas-6(L69T)* mutation.

498 **Discussion**

499 Through our studies, we have re-created the MCPH-associated *sas-6(L69T)* mutation in *C.*
500 *elegans* by CRISPR to generate the first *C. elegans* model of a MCPH-associated mutation. A
501 previous study investigated the effects of the human SASS6(I62T) mutation (the human
502 equivalent of the SAS-6(L69T) mutation) on centrosome duplication in U2OS cells (Khan et al.
503 2014). In their studies, the authors noted an inhibition of centrosome duplication in U2OS cells
504 expressing the SASS6(I62T) protein from exogenous plasmid constructs carrying the
505 *SASS6(I62T)* mutation. The levels of SASS6 in the cell must be tightly regulated for its proper
506 cellular function. Either overexpressing the SASS6 protein or depleting it can affect proper
507 centrosome duplication (Dammermann et al. 2004, Leidel et al. 2005). Therefore, to investigate
508 the effect of the *sas-6(L69T)* mutation on centrosome duplication in an endogenous context, we
509 monitored centrosome duplication in our *sas-6(L69T)* CRISPR worm model. Interestingly, *C.*
510 *elegans* carrying this mutation appeared phenotypically wild-type and did not exhibit any defects
511 in embryonic viability or brood size **(Figure 2)**. *C. elegans* embryonic divisions are reliant on
512 proper centrosome duplication. Since we did not detect any embryonic lethality in the presence
513 of the *sas-6(L69T)* mutation **(Figure 2B)**, we concluded that centrosome duplication is likely to
514 be relatively unaffected in the *sas-6(L69T)* mutant worms in a wild-type background.

515 To uncover the potential milder effects of this mutation on centrosome duplication that
516 may not be visible in a wild-type genetic background, we introduced this mutation in the
517 sensitized *zyg-1(it25)* background. Interestingly, the *sas-6(L69T)* mutation significantly
518 enhanced the centrosome duplication failures and embryonic lethality of *zyg-(it25)* worms
519 **(Figures 3B, 3C, 3D)**. These data demonstrate that the MCPH-associated *sas-6(L69T)*
520 mutation does, in fact, reduce SAS-6 function in regulating centrosome duplication. However,

521 this effect can only be revealed in a sensitized genetic background. Thus, at least in the context
522 of this MCPH-associated mutation, centrosome duplication is only mildly affected by this
523 mutation. Future studies will involve elucidating the molecular mechanism by which the *sas-*
524 *6(L69T)* mutation inhibits centrosome duplication.

525 Our data that the *sas-6(L69T)* mutation likely has a mild effect on SAS-6 function in
526 regulating centrosome duplication are consistent with the observed phenotypic effects of the
527 *SASS6(I62T)* mutation in human MCPH patients. *SASS6*/*sas-6* is an essential gene that is
528 required for proper centrosome duplication and cell division (Kamath et al. 2003, Dammermann
529 et al. 2004, Leidel et al. 2005, Blomen et al. 2015). If the *SASS6(I62T)* mutation severely
530 inhibited SASS6 function in regulating centrosome duplication, it would be expected to result in
531 embryonic lethality. As a result, there would not be human patients living with homozygous
532 copies of the *SASS6(I62T)* mutation. However, the fact that there are *SASS(I62T)* homozygous
533 individuals in the population (Khan et al. 2014) indicates that this mutation does not severely
534 perturb SASS6 role in regulating centrosome duplication in humans. Therefore, our data in *C.*
535 *elegans* which demonstrate that embryonic viability is unaffected in the presence of this
536 mutation **(Figure 2B)** are in line with the observations in human MCPH patients carrying this
537 mutation.

538 Modeling the L69T mutation using AlphaFold2 did not reveal any significant changes in
539 the structure of the SAS-6 protein **(Figures 4B, 4C)**. This is not a surprising finding since *sas-6*
540 is an essential gene and therefore severely affecting SAS-6 structure may alter centriole
541 architecture and result in embryonic lethality. However, our AlphaFold2 analysis revealed that a
542 deep hydrophobic pocket within SAS-6 is altered by the *sas-6(L69T)* mutation **(Figures 4B, 4C,**
543 **dark blue arrows)**. Presently, no known function has been ascribed to this hydrophobic pocket
544 in SAS-6. Based upon our data, we are tempted to speculate that this SAS-6 hydrophobic

545 pocket may mediate an as-yet unknown interaction of SAS-6 with a protein(s) that may be
546 important for its function in ciliogenesis, dendrite morphogenesis and/or centrosome duplication.

547 The effect of the *SASS6(I62T)* mutation on ciliogenesis has not been investigated. Upon
548 introducing the *sas-6(L69T)* mutation into a pan-ciliary marker expressing *C. elegans* strain, we
549 determined that ciliogenesis is perturbed in the *sas-6(L69T)* mutant worms **(Figures 5C, 5D,**
550 **6B, 6C, 6D)**. Specifically, the *sas-6(L69T)* worms have shorter phasmid cilia and a defective
551 phasmid cilia morphology **(Figures 5C, 5D, 6B, 6C, 6D)**. Ciliogenesis defects have been
552 associated with the incidence of microcephaly (Alcantara et al. 2014, Gabriel et al. 2016, Broix
553 et al. 2018, Wambach et al. 2018, Zhang et al. 2019, Ding et al. 2019, Sohayeb et al. 2020,
554 Farooq et al. 2020). Interestingly, in a study by Shohayeb et al., the authors determined that
555 mouse embryonic fibroblasts that were derived from WDR62 mutant mice carrying CRISPR-
556 edited MCPH patient mutations exhibited a shortened ciliary length, like we report here
557 (Shohayeb et al. 2019). In another study, Wambach et al. cultured MCPH patient derived
558 fibroblasts and found that these fibroblasts had shorter primary cilia than those of fibroblasts
559 that were cultured from a healthy control individual (Wambach et al. 2018). Thus, there is
560 precedence for shorter ciliary length being associated with MCPH.

561 Our data indicate that SAS-6 levels are reduced in *sas-6(L69T)* worms in a *zyg-1(it25)*
562 background but not in an otherwise wild-type background **(Figure S1)**. Since we observe
563 ciliogenesis defects in the presence of the *sas-6(L69T)* mutation even in a wild-type background
564 (Figures 5C, 5D, 6B, 6C, 6D), we propose that decreased SAS-6 levels are likely not sufficient
565 to explain the effects of the *sas-6(L69T)* mutation.

566 We find that in *C. elegans* carrying the *sas-6(L69T)* mutation, centrosome duplication
567 defects can only be detected in a sensitized *zyg-1(it25)* genetic background **(Figures 3B, 3C).**
568 However, the ciliogenesis and dendritic defects induced by this mutation can be uncovered
569 even in an otherwise wild-type background **(Figures 5C, 5D, 6B, 6C, 6D)**. These findings lead

570 us to speculate that perhaps, at least in the context of this specific MCPH-associated mutation,
571 the inhibition of proper ciliogenesis may be a more important contributor to the development of
572 MCPH than the inhibition of centrosome duplication. However, it is also possible that the
573 centrosome duplication and ciliogenesis defects induced by this mutation synergize to cause
574 MCPH in human patients carrying this mutation. In the future, it will be interesting to determine if
575 the *SASS6(I62T)* mutation also affects ciliogenesis in human cell lines. It will also be interesting
576 to examine if other such MCPH-associated mutations likewise affect ciliogenesis in addition to
577 affecting centrosome duplication.

578 Since *sas-6* is an essential gene, many *sas-6* mutant alleles are difficult to maintain and
579 analyze (O'Rourke et al. 2011, Song et al. 2011, The C. elegans Deletion Mutant Consortium et
580 al. 2012, Lettman et al. 2013). This has made it tedious to dissect the function of SAS-6 in
581 ciliogenesis. A previous study expressed a *sas-6* sgRNA and Cas9 protein using a heat-shock
582 promoter to demonstrate that SAS-6 plays a critical role in *C. elegans* ciliogenesis (Li et al.
583 2017). However, the mechanistic investigation of these defects has been challenging due to the
584 high lethality and sterility of *sas-6* mutant alleles. Notably, our studies indicate that *sas-6(L69T)*
585 mutant worms appear phenotypically wild-type and yet exhibit significant ciliogenesis defects.
586 Therefore, we expect that our *sas-6(L69T)* CRISPR strain will be a useful tool to unravel the
587 mechanism by which SAS-6 regulates ciliogenesis. In the future, forward genetic screens can
588 be performed with the *sas-6(L69T)* allele to identify additional genes that may genetically
589 interact with *sas-6* to regulate ciliogenesis in the worm.

590 Our data indicate that *C. elegans* harboring the *sas-6(L69T)* mutation also exhibit
591 sensory neuronal defects such as a shortened dendrite length **(Figure 7)**. This is a surprising
592 finding since *C. elegans* centrioles have been found to degenerate during neuronal
593 differentiation (Li et al. 2017, Serwas et al. 2017, Nechipurenko et al. 2017). One possibility is
594 that SAS-6 functions independently of its role as a core centriolar protein in regulating dendrite

595 length in *C. elegans* sensory neurons. Another possibility is that SAS-6 function at the centrioles
596 may be required for proper phasmid dendrite extension through an unknown mechanism. In the
597 future, transmission electron microscopy analysis of dendrites and cilia from *sas-6(L69T)* mutant
598 worms should be performed to determine the nature of the dendritic and ciliary defects in these
599 mutant worms. Future studies will also involve analyzing *C. elegans* strains expressing a variety
600 of fluorescently-tagged markers (e.g. Intraflagellar transport markers, transition zone markers,
601 neuron-specific markers, etc.) to further dissect the mechanism by which the *sas-6(L69T)*
602 mutation affects ciliogenesis and dendrite extension.

603 Defective chemotaxis towards butanone was seen in *C. elegans* carrying the *sas-*
604 *6(L69T)* mutation **(Figure 8).** Future studies should also be directed towards examining what
605 other worm behaviors (if any) are altered in *C. elegans* carrying the *sas-6(L69T)* mutation. It is
606 important to note that in this study, we have only examined the effect of the *sas-6(L69T)*
607 mutation on ciliogenesis and behaviors in the *C. elegans* hermaphrodite. The effect of this
608 mutation on *C. elegans* males is unknown. Assays such as male mating assays could be carried
609 out in the future to determine if male-specific behaviors are affected by the *sas-6(L69T)*
610 mutation.

611 As our *C. elegans* model of the *sas-6(L69T)* mutation recapitulates many of the effects
612 seen in the human MCPH patients carrying this mutation, we expect that *C. elegans* will be
613 more widely adopted as a model system to study the effects of additional MCPH-associated
614 human mutations in the future.

615 **Figure 1. The MCPH-associated *sas-6(L69T)* mutation was successfully generated in *C.***
616 ***elegans* by CRISPR/Cas9 editing** A) Schematic of the CRISPR repair template used for
617 inserting the leucine to threonine mutation at amino acid 69 of the *C. elegans* SAS-6 protein
618 (Note: Only 10 out of 45 bases of the 5' and 3' homology ends of the repair template are
619 shown). The teal highlights represent bases that are identical between the repair template and

620 the *sas-6* gene sequence. The magenta highlight indicates the bases that were altered to
621 introduce the leucine 69 to threonine mutation into the endogenous *sas-6* gene. The bases
622 highlighted in gray represent silent mutations that were introduced in the repair template to
623 prevent its cutting by the Cas9 enzyme. B) Agarose gel electrophoresis of PCR products
624 digested with EcoRI to screen for homozygous-edited *C. elegans* carrying the *sas-6(L69T)*
625 mutation. Black stars: Homozygous-edited worms; het: heterozygote; WT: wild-type.

626 **Figure 2. The *sas-6(L69T)* mutation does not affect *C. elegans* brood size or embryonic**
627 **viability.** A) Brood sizes of wild-type and *sas-6(L69T)* mutant worms were determined at
628 temperatures of 16°C, 20°C and 25°C. Each circle or triangle represents the brood size of a
629 single adult hermaphrodite. No statistically significant difference in brood size was observed
630 between wild-type and *sas-6(L69T)* worms at any of the assessed temperatures. n= number of
631 worms whose brood was analyzed for each strain. n.s: not significant. Error bars represent the
632 standard deviation. The middle bar represents the mean. B) Embryonic viability of wild-type and
633 *sas-6(L69T)* worms was analyzed at temperatures of 16°C, 20°C and 25°C. Each circle or
634 triangle represents the embryonic viability of a single adult hermaphrodite. The middle line
635 represents the median embryonic viability with a 95% confidence interval. No major change in
636 embryonic viability was observed between wild-type and *sas-6(L69T)* worms at any of the
637 assessed temperatures. The viability of over 2000 embryos was analyzed for each strain at
638 every temperature.

639 **Figure 3. The *sas-6(L69T)* mutation increases the centrosome duplication failures and the**
640 **embryonic lethality of *zyg-1(it25)* worms.** A) Schematic showing the genetic cross that was
641 performed to combine the *sas-6(L69T)* mutation with the *zyg-1(it25)* mutation. B) Stills from
642 time-lapse imaging of *zyg-1(it25)* and *zyg-1(it25);sas-6(L69T)* strains expressing fluorescently-
643 tagged centrosome and DNA markers. Grayscale: mCherry-SPD-2 (centrosome marker);
644 Green: GFP-histone (DNA marker). In a majority of *zyg-1(it25)* mutant embryos, centrosome

645 duplication proceeds normally at a semi-permissive temperature of 21.8°C, yielding two
646 centrosomes in each cell of a 2-cell *C. elegans* embryo (**Figure 3B, top panel, white arrows**).
647 Scale bar = 10 µm. On the contrary, most of the *zyg-1(it25);sas-6(L69T)* mutant centrosomes
648 fail to duplicate at 21.8°C resulting in a single centrosome present in each cell of a 2-cell *C.*
649 *elegans* embryo (**Figure 3B, bottom panel, white arrows**). C) Quantification of B). n= number
650 of centrosomes analyzed. Approximately 83% of the *zyg-1(it25)* centrosomes duplicate normally
651 at 21.8°C. In contrast, only about 28% of the *zyg-1(it25);sas-6(L69T)* centrosomes duplicate
652 normally at this temperature. D) Quantification of embryonic viability of *zyg-1(it25)* single and
653 *zyg-1(it25);sas-6(L69T)* double mutants at the semi-permissive temperature of 21.7°C. Average
654 embryonic viability is reduced from ~44% to ~7% in the presence of the *sas-6(L69T)* mutation.
655 The viability of 1103 embryos from *zyg-1(it25)* worms and 912 embryos from *zyg-1(it25);sas-*
656 *6(L69T)* worms was analyzed. Embryos from 18 worms were analyzed for each condition.
657 Unpaired two-tailed t-test, $p<0.0001$. Error bars represent the standard deviation and the middle
658 bar represents the mean.

659 **Figure 4. The L69T mutation does not significantly alter the overall structure of the *C.***
660 ***elegans* SAS-6 protein.** A) Cartoon depicting the location of the L69T mutation within the *C.*
661 *elegans* SAS-6 protein oriented with respect to known SAS-6 protein domains and SAS-6 amino
662 acid residues that are important for the interaction of SAS-6 with either itself or with other known
663 interactors (Kitagawa et al. 2011, Lettman et al. 2013). B) Structure of *C. elegans* SAS-6 protein
664 (PDB accession number: 4G79, Hilbert et al. 2013) C) The *C. elegans* SAS-6(L69T) protein
665 structure was modeled using AlphaFold2. The coloring for the models are based on the
666 ChimeraX default palette-option where lipophilicity ranges from -20 to 20 going from cyan (least
667 lipophilic) to golden (most lipophilic). Blue arrows: A deep hydrophobic pocket within the mutant
668 SAS-6(L69T) protein is decreased by the L69T mutation.

669 **Figure 5. Phasmid cilia length is shorter in *sas-6(L69T)* mutant worms.** A) A schematic of
670 the genetic crossing experiment that was performed to introduce the MCPH-associated *sas-*
671 *6(L69T)* mutation into the PY6100 pan-ciliary marker strain. B) Cartoon showing the anatomical
672 positioning of a *C. elegans* phasmid cilium and dendrite within the tail region of the worm. C) Z-
673 projection confocal images of phasmid neurons from *osm-6p::gfp* (top panel) and *osm-6p::gfp;*
674 *sas-6(L69T)* (bottom panel) worms highlighting the difference in phasmid cilia lengths between
675 the two genotypes. On average, control *osm-6p::gfp* worms have longer phasmid cilia (top
676 panel, white bracket) than *osm-6p::gfp;sas-6(L69T)* worms (bottom panel, white bracket). White
677 brackets denote the cilia. Scale bar = 10 μm. D) Quantification of phasmid cilia lengths of
678 control (*osm-6p::gfp*) and *sas-6(L69T)* (*osm-6p::gfp;sas-6(L69T)*) worms. Each circle represents
679 the length of a single phasmid cilium. n= number of phasmid cilia analyzed for each genotype.
680 Phasmid cilia length was reduced from 5.82 μm in control worms (n=54) to 3.99 μm in *osm-*
681 *6p::gfp;sas-6(L69T)* worms (n=59). $p<0.0001$, unpaired two-tailed t-test. The error bars
682 represent the standard deviation and the middle bar represents the mean.

683 **Figure 6. Phasmid cilia morphology is defective in a subset of the *sas-6(L69T)* mutant**
684 **worms.** A) Cartoon showing the organization of a typical phasmid neuron with a ciliary
685 axoneme (A) built on top of the transition zone (TZ). The dendrite of the phasmid neuron
686 connects to the TZ. B) and C) Representative Z-projection confocal images of phasmid cilia
687 morphology in *osm-6p::gfp* and *osm-6p::gfp;sas-6(L69T)* worms, respectively. B) *osm-6p::gfp*
688 worms have a stereotypical phasmid cilia morphology with two prominent TZs at the base and
689 ciliary axonemes projecting from the TZs. Scale bar = 10 μm. C) A subset of the *osm-6p::gfp;*
690 *sas-6(L69T)* worms exhibit deformed phasmid cilia morphologies. Scale bar = 10 μm. D)
691 Quantification of B) and C). While all of the control (*osm-6p::gfp)* phasmid neurons (n=61)
692 exhibit a normal phasmid cilia morphology, 15.4% of the analyzed *osm-6p::gfp;sas-6(L69T)*

693 phasmid neurons show a deformed cilia morphology (n=65). n= number of phasmid neurons
694 analyzed. p=0.0014, Fisher's exact test.

695 **Figure 7. Dendrite length is shorter in *osm-6p::gfp;sas-6(L69T)* phasmid neurons.** A)
696 Representative Z-projection confocal image of the average phasmid dendrite length in *osm-*
697 *6p::gfp* worms. Scale bar = 10 µm. B) Representative Z-projection confocal image of the
698 average phasmid dendrite length in *osm-6p::gfp;sas-6(L69T)* worms. Scale bar = 10 µm. C)
699 Quantification of A) and B). The average dendrite length of control (*osm-6p::GFP*) worms is 37.4
700 µm (n=38) while that of *osm-6p::gfp;sas-6(L69T)* worms is 28.1 µm (n=42). n= number of
701 phasmid dendrites analyzed. p<0.0001, unpaired two-tailed t-test. The error bars and middle bar
702 represent the standard deviation and the mean, respectively.

703 **Figure 8. The *sas-6(L69T)* mutation reduces *C. elegans* chemotaxis to 1:500 Butanone.** A)
704 Schematic of chemotaxis assay experiments. L4 stage *C. elegans* were plated onto unseeded
705 NGM plates that had been divided into four quadrants, two with solvent (ethanol) and two with
706 odorant (1:500 butanone in ethanol). The worms were placed in the center of the plate and
707 allowed to move around for 1 hour at 25°C. After 1 hour, the number of worms in each quadrant
708 were counted and quantified. The formula C.I. = (# animals in two odorant quadrants)/(#
709 animals in any of the four quadrants) was used to compute the Chemotaxis Index (C.I.). Worms
710 on any line or within the origin were not counted. Four plates were used for each genotype per
711 experiment. Assays were repeated in triplicate. B) Quantification of data obtained from A). The
712 *sas-6(L69T)* mutants exhibit a decreased chemotaxis towards 1:500 butanone as compared
713 with control worms. n= Number of worms whose chemotaxis towards 1:500 butanone was
714 analyzed. p<0.0001, unpaired two-tailed t-test. C) Summary of data from A) The average
715 chemotaxis index of *sas-6(L69T)* worms was 0.3307. This chemotaxis index was less than the
716 average chemotaxis index of control worms which was 0.4107. C.I.=Chemotaxis Index.

717 **Supplementary Figures**

718 **Figure S1. SAS-6 protein levels are slightly reduced in the presence of the *sas-6(L69T)***
719 **mutation in a *zyg-1(it25)* background but are unaffected in a wild-type background.** A) A
720 representative western blot image of an HA blot showing SAS-6 levels in *zyg-1(it25);sas-6::ha*
721 and *zyg-1(iti25);sas-6(L69T)::ha* worms. Tubulin served as a loading control. SAS-6 protein
722 levels are slightly decreased in the presence of the *sas-6(L69T)* mutation in a *zyg-1(it25)*
723 background B) Quantification of A) from four independent experiments. On average, SAS-6
724 protein levels are reduced by 15% in the presence of the *sas-6(L69T)* mutation in the *zyg-1(it25)*
725 background. P=0.0475, unpaired two-tailed t-test. C) A representative western blot image of a
726 HA blot showing SAS-6 levels in *sas-6::ha* and *sas-6(L69T)::ha* worms. Tubulin was used as a
727 loading control. Although SAS-6 protein levels tend to decrease in the presence of the *sas-*
728 *6(L69T)* mutation in a wild-type background, this decrease is not statistically significant
729 (p=0.1398, unpaired two-tailed t-test).

730 **Data Availability Statement**

731 All the strains made and used in this study will be made available upon request. **Table S1** lists
732 all the strains made in this study.

733 **Acknowledgments**

734 We would like to thank the Sengupta lab for providing the PY6100 strain that was used for cilia
735 analysis. We would like to thank the O'Connell lab for providing the OC14 and OC869 strains
736 that have been used in this study. The wild-type N2 Bristol strain was provided by the CGC,
737 which is funded by NIH Office of Research Infrastructure Programs (P40 OD010440). We would
738 like to acknowledge Peter Nunan and Mariah Moreland for their technical assistance. Adam
739 Norris received funding from NIH R35GM133461. Finally, we would like to thank Drs. Steve
740 Caplan and Nina Peel for their critical comments on this manuscript.

741 **Funding**

742 The authors would like to acknowledge the National Institute of General Medical Sciences
743 (NIGMS) of the National Institutes of Health (NIH) for grant support 5P20GM103636-09,
744 University of Tulsa (TU) Start-up funding, the TU Faculty Summer Development Fellowship and
745 Shark Tank Grant awarded to Jyoti Iyer. Amy Smith, Mary Bergwell, Ellie Smith, Carter Dierlam,
746 Ramon Duran and Rory Seidel received funding and research support from the TU Chemistry
747 Summer Undergraduate Research Program and/or from the Tulsa Undergraduate Research
748 Challenge program. Ellie Smith and Carter Dierlam also received financial support from the
749 NIGMS grant 5P20GM103636-09 awarded to Jyoti Iyer.

750 **Conflict of Interest**

751 The authors declare no competing interests.

752 **References**

753 Abràmoff MD, Magalhães PJ, Ram SJ. 2004. Image processing with ImageJ. Biophotonics
754 Int. 11(7):36-42.
755 Alcantara D, O'Driscoll M. Congenital microcephaly. 2014. Am J Med Genet C Semin Med
756 Genet. 166(2):124-139.
757 Arribere JA, Bell RT, Fu BX, Artiles KL, Hartman PS, Fire AZ. 2014. Efficient marker-free
758 recovery of custom genetic modifications with CRISPR/Cas9 in Caenorhabditis
759 elegans. Genetics. 198(3):837-846.
760 Bargmann CI, Hartwieg E, Horvitz HR. 1993. Odorant-selective genes and neurons mediate
761 olfaction in C. elegans. Cell. 74(3):515-527.
762 Bayer EA, Sun H, Rafi I, Hobert O. 2020. Temporal, spatial, sexual and environmental
763 regulation of the master regulator of sexual differentiation in C. elegans. Curr Biol.
764 30(18):3604-3616.
765 Bergwell M, Smith A, Lakin H, Slay R, Iyer J. 2019. Generation of sas-6:: ha by CRISPR/Cas9

766 editing. MicroPubl Biol. 2019.
767 Bettencourt-Dias M, Rodrigues-Martins A, Carpenter L, Riparbelli M, Lehmann L, Gatt
768 MK, Carmo N, Balloux F, Callaini G, Glover DM. 2005. SAK/PLK4 is required for
769 centriole duplication and flagella development. Curr Biol. 15(24):2199-2207.
770 Blomen VA, Májek P, Jae LT, Bigenzahn JW, Nieuwenhuis J, Staring J, Sacco R, van
771 Diemen FR, Olk N, Stukalov A, et al. 2015. Gene essentiality and synthetic lethality in
772 haploid human cells. Science. 350(6264):1092-1096.
773 Broix L, Asselin L, Silva CG, Ivanova EL, Tilly P, Gilet JG, Lebrun N, Jagline H, Muraca G,
774 Saillour Y, et al. 2018. Ciliogenesis and cell cycle alterations contribute to KIF2A-related
775 malformations of cortical development. Hum Mol Genet. 27(2):224-238.
776 Broto P, Moreau G, Vandycke C. 1984. Molecular structures: perception, autocorrelation
777 descriptorand sar studies: system of atomic contributions for the calculation of the n-
778 octanol/water partition coefficients. Eur J Med Chem. 19(1):71-78.
779 Busch J, Erat MC, Blank ID, Musgaard M, Biggin PC, Vakonakis I. 2019. A dynamically
780 interacting flexible loop assists oligomerisation of the Caenorhabditis elegans centriolar
781 protein SAS-6. Sci Rep. 9(1):1-11.
782 Collet J, Spike CA, Lundquist EA, Shaw JE, Herman RK. 1998. Analysis of osm-6, a gene that
783 affects sensory cilium structure and sensory neuron function in Caenorhabditis elegans.
784 Genetics. 148(1):187-200.
785 Dammermann A, Müller-Reichert T, Pelletier L, Habermann B, Desai A, Oegema K. 2004.
786 Centriole assembly requires both centriolar and pericentriolar material proteins. Dev
787 Cell. 7(6):815-829.
788 Delattre M, Canard C, Gönczy P. 2006. Sequential protein recruitment in C. elegans centriole
789 formation. Curr Biol. 16(18):1844-1849.
790 Ding W, Wu Q, Sun L, Pan NC, Wang X. 2019. Cenpj regulates cilia disassembly and
791 neurogenesis in the developing mouse cortex. J Neurosci. 39(11):1994-2010.

792 Drummond IA. 2012. Cilia functions in development. Curr Opin Cell Biol. 24(1):24-30.
793 Farooq M, Lindbæk L, Krogh N, Doganli C, Keller C, Mönnich M, Gonçalves AB,
794 Sakthivel S, Mang Y, Fatima A, et al. 2020. RRP7A links primary microcephaly to
795 dysfunction of ribosome biogenesis, resorption of primary cilia, and neurogenesis. Nat
796 Commun. 11(1):1-6.
797 Gabriel E, Wason A, Ramani A, Gooi LM, Keller P, Pozniakovsky A, Poser I, Noack F,
798 Telugu NS, Calegari F, et al. 2016. CPAP promotes timely cilium disassembly to
799 maintain neural progenitor pool. EMBO J. 35(8):803-819.
800 Habedanck R, Stierhof YD, Wilkinson CJ, Nigg EA. 2005. The Polo kinase Plk4 functions in
801 centriole duplication. Nat Cell Biol. 7(11):1140-1146.
802 Hilbert M, Erat MC, Hachet V, Guichard P, Blank ID, Flückiger I, Slater L, Lowe ED,
803 GN, Steinmetz MO, et al. 2013. Caenorhabditis elegans centriolar protein SAS-6 forms a
804 spiral that is consistent with imparting a ninefold symmetry. Proc Natl Acad Sci U S A.
805 110(28):11373-11378.
806 Inglis PN, Ou G, Leroux MR, Scholey JM. 2007. The sensory cilia of Caenorhabditis elegans.
807 WormBook, ed. The C. elegans Research Community. Wormbook. 1-22.
808 Iyer J, DeVaul N, Hansen T, Nebenfuehr B. 2019. Using microinjection to generate genetically
809 modified Caenorhabditis elegans by CRISPR/Cas9 Editing. In Microinjection. Humana
810 Press, New York, NY. 431-457.
811 Jumper J, Evans R, Pritzel A, Green T, Figurnov M, Ronneberger O, Tunyasuvunakool K, Bates
812 R, Žídek A, Potapenko A, et al. 2021. Highly accurate protein structure prediction with
813 AlphaFold. Nature. 596(7873):583-589.
814 Kamath RS, Fraser AG, Dong Y, Poulin G, Durbin R, Gotta M, Kanapin A, Le Bot N,
815 Moreno S, Sohrmann M, et al. 2003. Systematic functional analysis of the
816 Caenorhabditis elegans genome using RNAi. Nature. 421(6920):231-237.
817 Kemp CA, Song MH, Addepalli MK, Hunter G, O'Connell K. 2007. Suppressors of zyg-1 define

818 regulators of centrosome duplication and nuclear association in Caenorhabditis elegans.
819 Genetics. 176(1):95-113.
820 Kemphues KJ, Kusch M, Wolf N. 1988. Maternal-effect lethal mutations on linkage group II of
821 Caenorhabditis elegans. Genetics. 120(4):977-986.
822 Khan MA, Rupp VM, Orpinell M, Hussain MS, Altmüller J, Steinmetz MO, Enzinger C,
823 Thiele H, Höhne W, Nürnberg G, Baig SM. 2014. A missense mutation in the PISA
824 domain of HsSAS-6 causes autosomal recessive primary microcephaly in a large
825 consanguineous Pakistani family. Hum Mol Genet. 23(22):5940-5949.
826 Kitagawa D, Vakonakis I, Olieric N, Hilbert M, Keller D, Olieric V, Bortfeld M, Erat MC, Flückiger
827 I, Gönczy P, et al. 2011. Structural basis of the 9-fold symmetry of centrioles. Cell.
828 144(3):364-375.
829 Laguerre ML, Saux M, Dubost JP, Carpy A. 1997. MLPP: a program for the calculation of
830 molecularlipophilicity potential in proteins. Pharm. Sci. 3.5–6:217–222.
831 Leidel S, Delattre M, Cerutti L, Baumer K, Gönczy P. 2005. SAS-6 defines a protein family
832 required for centrosome duplication in C. elegans and in human cells. Nat Cell Biol.
833 7(2):115-125.
834 Lettman MM, Wong YL, Viscardi V, Niessen S, Chen SH, Shiau AK, Zhou H, Desai A,
835 Oegema K. 2013. Direct binding of SAS-6 to ZYG-1 recruits SAS-6 to the mother
836 centriole for cartwheel assembly. Dev cell. 25(3):284-298.
837 Levine MS, Bakker B, Boeckx B, Moyett J, Lu J, Vitre B, Spierings DC, Lansdorp PM,
838 Cleveland DW, Lambrechts D, et al. 2017. Centrosome amplification is sufficient to
839 promote spontaneous tumorigenesis in mammals. Dev cell. 40(3):313-322.
840 Li W, Yi P, Zhu Z, Zhang X, Li W, Ou G. 2017. Centriole translocation and degeneration
841 during ciliogenesis in Caenorhabditis elegans neurons. EMBO J. 36(17):2553-2566.
842 Liang X, Calovich-Benne C, Norris A. 2022. Sensory neuron transcriptomes reveal complex

843 neuron-specific function and regulation of mec-2/Stomatin splicing. Nucleic Acids Res.
844 50(5):2401-2416.
845 Martin CA, Ahmad I, Klingseisen A, Hussain MS, Bicknell LS, Leitch A, Nürnberg G,
846 Toliat MR, Murray JE, Hunt D, et al. 2014. Mutations in PLK4, encoding a master
847 regulator of centriole biogenesis, cause microcephaly, growth failure and retinopathy.
848 Nat Genet. 46(12):1283-1292.
849 Mirdita M, Schütze K, Moriwaki Y, Heo L, Ovchinnikov S, Steinegger M. 2022. ColabFold:
850 making protein folding accessible to all. Nat Methods. 30:1-4.
851 Nechipurenko IV, Berciu C, Sengupta P, Nicastro D. 2017. Centriolar remodeling underlies
852 basal body maturation during ciliogenesis in Caenorhabditis elegans. Elife. 6:e25686.
853 Nigg EA, Holland AJ. 2018. Once and only once: mechanisms of centriole duplication and
854 their deregulation in disease. Nat Rev Mol Cell Biol. 19(5):297-312.
855 O'Rourke SM, Yochem J, Connolly AA, Price MH, Carter L, Lowry JB, Turnbull DW,
856 Kamps-Hughes N, Stiffler N, Miller MR, et al. 2011. Rapid mapping and identification of
857 mutations in Caenorhabditis elegans by restriction site-associated DNA mapping and
858 genomic interval pull-down sequencing. Genetics. 189(3):767-778.
859 O'Connell KF, Caron C, Kopish KR, Hurd DD, Kemphues KJ, Li Y, White JG. 2001. The C.
860 elegans zyg-1 gene encodes a regulator of centrosome duplication with distinct maternal
861 and paternal roles in the embryo. Cell. 105(4):547-558.
862 Paix A, Folkmann A, Rasoloson D, Seydoux G. 2015. High efficiency, homology-directed
863 genome editing in Caenorhabditis elegans using CRISPR-Cas9 ribonucleoprotein
864 complexes. Genetics. 201(1):47-54.
865 Paix A, Schmidt H, Seydoux G. 2016. Cas9-assisted recombineering in C. elegans: genome
866 editing using in vivo assembly of linear DNAs. Nucleic Acids Res. 44(15):e128.
867 Patwardhan D, Mani S, Passemard S, Gressens P, El Ghouzzi V. 2018. STIL balancing
868 primary microcephaly and cancer. Cell Death Dis. 9(2):65.

869 Peel N, Iyer J, Naik A, Dougherty MP, Decker M, O'Connell KF. 2017. Protein phosphatase 1
870 down regulates ZYG-1 levels to limit centriole duplication. PLoS Genet. 13(1):e1006543.
871 Pelletier L, O'Toole E, Schwager A, Hyman AA, Müller-Reichert T. 2006. Centriole assembly in
872 Caenorhabditis elegans. Nature. 444(7119):619-623.
873 Perkins LA, Hedgecock EM, Thomson JN, Culotti JG. 1986. Mutant sensory cilia in the
874 nematode Caenorhabditis elegans. Dev Biol. 117(2):456-487.
875 Phan TP, Holland AJ. 2021. Time is of the essence: the molecular mechanisms of primary
876 microcephaly. Genes Dev. 35(23-24):1551-1578.
877 Piano F, Schetter AJ, Mangone M, Stein L, Kemphues KJ. 2000. RNAi analysis of genes
878 expressed in the ovary of Caenorhabditis elegans. Curr Biol. 10(24):1619-1622.
879 Power KM, Akella JS, Gu A, Walsh JD, Bellotti S, Morash M, Zhang W, Ramadan YH,
880 Ross N, Golden A, et al. 2020. Mutation of NEKL-4/NEK10 and TTLL genes suppress
881 neuronal ciliary degeneration caused by loss of CCPP-1 deglutamylase function. PLoS
882 Genet. 16(10):e1009052.
883 Qiao R, Cabral G, Lettman MM, Dammermann A, Dong G. 2012. SAS-6 coiled-coil structure
884 and interaction with SAS-5 suggest a regulatory mechanism in C. elegans centriole
885 assembly. EMBO J. 31(22):4334-4347.
886 Serwas D, Su TY, Roessler M, Wang S, Dammermann A. 2017. Centrioles initiate cilia
887 assembly but are dispensable for maturation and maintenance in C. elegans. J Cell Biol.
888 216(6):1659-1671.
889 Shohayeb B, Ho U, Yeap YY, Parton RG, Millard SS, Xu Z, Piper M, Ng DC. 2020. The
890 association of microcephaly protein WDR62 with CPAP/IFT88 is required for cilia
891 formation and neocortical development. Hum Mol Genet. 29(2):248-263.
892 Smith A, Bergwell M, Smith E, Mathew D, Iyer J. 2020. CRISPR/Cas9 Editing of the C.
893 elegans rbm-3.2 Gene using the dpy-10 Co-CRISPR Screening Marker and Assembled
894 Ribonucleoprotein Complexes. J Vis Exp. 166:e62001.

895 Song MH, Aravind L, Müller-Reichert T, O'Connell KF. 2008. The conserved protein SZY-20
896 opposes the Plk4-related kinase ZYG-1 to limit centrosome size. Dev Cell. 15(6):901-
897 912.
898 Song MH, Liu Y, Anderson DE, Jahng WJ, O'Connell KF. 2011. Protein phosphatase 2A-SUR-
899 6/B55 regulates centriole duplication in C. elegans by controlling the levels of
900 centriole assembly factors. Dev cell. 20(4):563-571.
901 The C. elegans Deletion Mutant Consortium, et al. 2012. Large-scale screening for targeted
902 knockouts in the Caenorhabditis elegans genome. G3 (Bethesda). 2(11):1415-1425.
903 van Breugel M, Hirono M, Andreeva A, Yanagisawa HA, Yamaguchi S, Nakazawa Y, Morgner
904 N, Petrovich M, Ebong IO, Robinson CV, et al. 2011. Structures of SAS-6 suggest its
905 organization in centrioles. Science. 331(6021):1196-1199.
906 Wambach JA, Wegner DJ, Yang P, Shinawi M, Baldridge D, Betleja E, Shimony JS, Spencer D,
907 Hackett BP, Andrews MV, et al. 2018. Functional characterization of biallelic RTTN
908 variants identified in an infant with microcephaly, simplified gyral pattern, pontocerebellar
909 hypoplasia, and seizures. Pediatr Res. 84(3):435-441.
910 Wilsch-Bräuninger M, Huttner WB. 2021. Primary Cilia and Centrosomes in Neocortex
911 Development. Front Neurosci. 15:755867.
912 Wolf B, Balestra FR, Spahr A, Gönczy P. 2018. ZYG-1 promotes limited centriole amplification
913 in the C. elegans seam lineage. Dev Biol. 434(2):221-230.
914 Xie S, Dierlam C, Smith E, Duran R, Williams A, Davis A, Mathew D, Naslavsky N, Iyer
915 J, Caplan S. 2022. The retromer complex regulates C. elegans development and
916 mammalian ciliogenesis. J Cell Sci. 135(10):jcs259396.
917 Zaqout S, Morris-Rosendahl D, Kaindl AM. 2017. Autosomal recessive primary microcephaly
918 (MCPH): an update. Neuropediatrics. 48(3):135-142.
919 Zhang W, Yang SL, Yang M, Herrlinger S, Shao Q, Collar JL, Fierro E, Shi Y, Liu A, Lu

920 H, et al. 2019. Modeling microcephaly with cerebral organoids reveals a WDR62–
921 CEP170–KIF2A pathway promoting cilium disassembly in neural progenitors. Nat
922 Commun. 10(1):1-4.
923
924

Figure 1

A

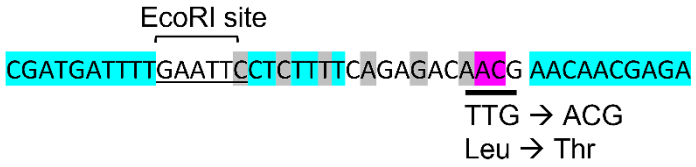
EcoRI site
CGATGATTTTGAATTCCTCTTTTCAGAGACAACG AACAACGAGA
TTG → ACG
Leu → Thr

B

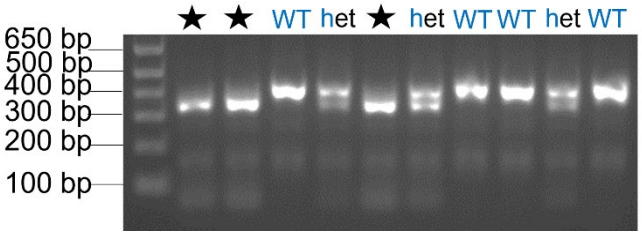
★ ★ WT het ★ het WT WT het WT
650 bp
500 bp
400 bp
300 bp
200 bp
100 bp

Figure 2

A

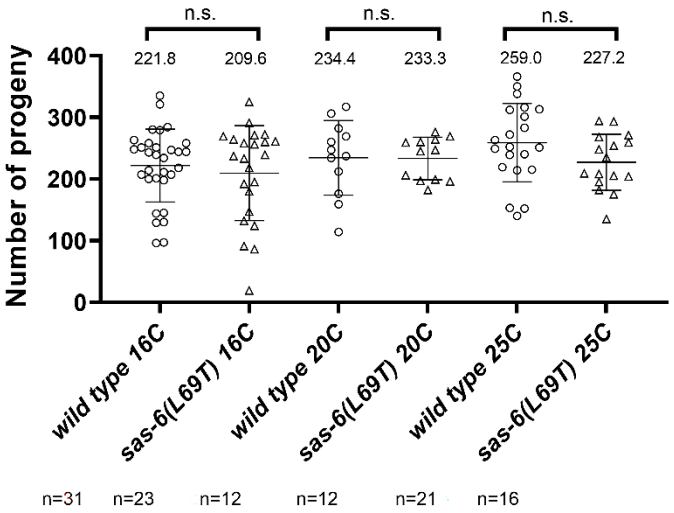
n.s.
n.s.
n.s.
221.8
209.6
234.4
233.3
259.0
227.2
Number of progeny
400
300
200
100
0
wild type 16C
sas-6(L69T) 16C
wild type 20C
sas-6(L69T) 20C
wild type 25C
sas-6(L69T) 25C
n=31
n=23
n=12
n=12
n=21
n=16

B

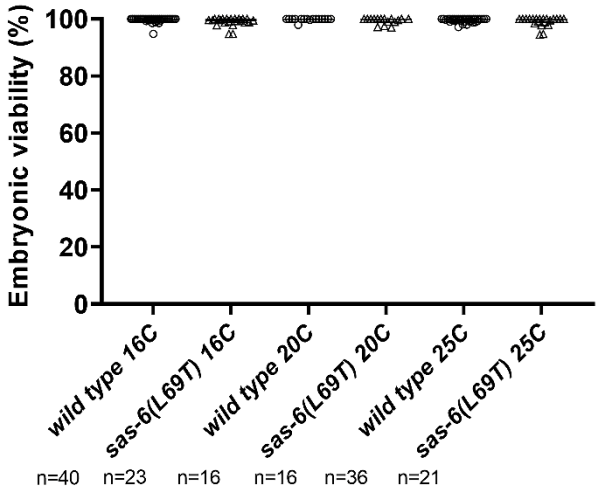
Embryonic viability (%)
100
80
60
40
20
0
wild type 16C
sas-6(L69T) 16C
wild type 20C
sas-6(L69T) 20C
wild type 25C
sas-6(L69T) 25C
n=40
n=23
n=16
n=16
n=36
n=21

Figure 3

A

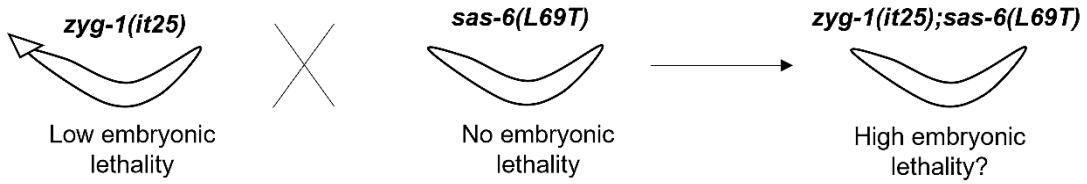

B

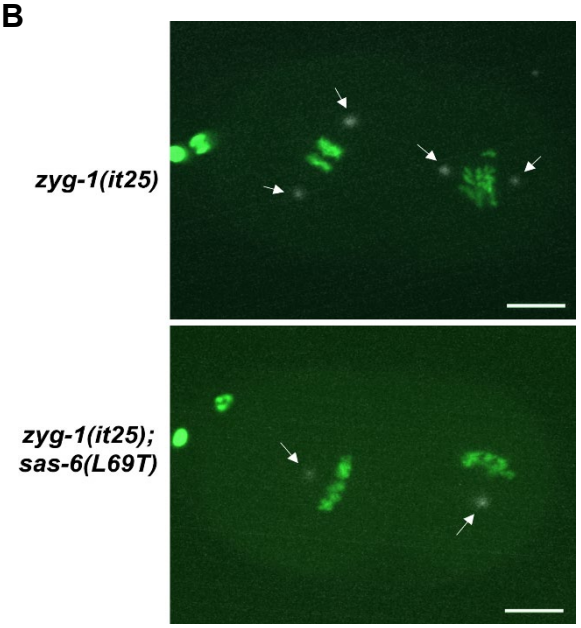

C

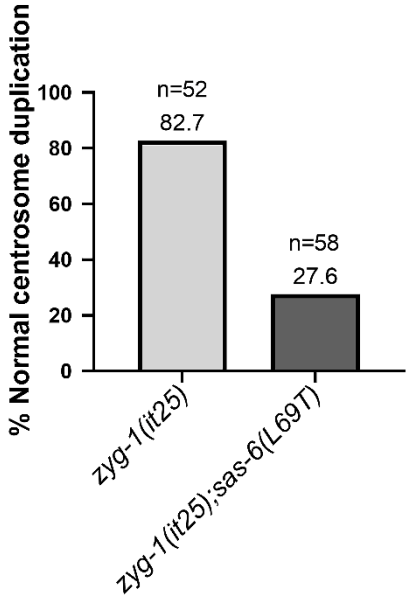

D

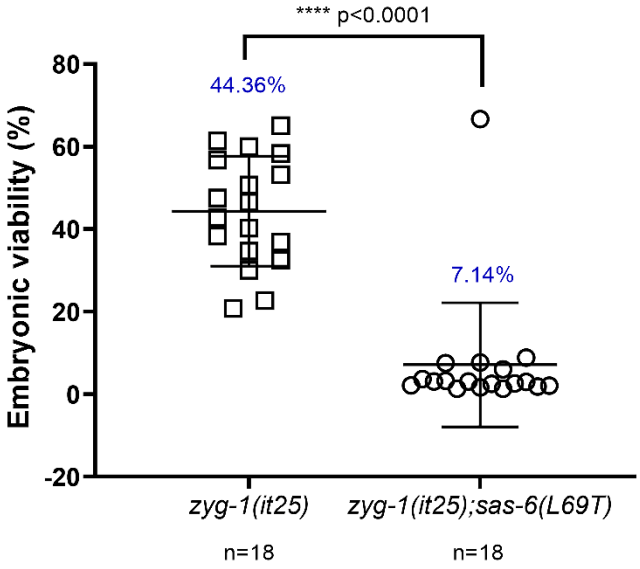

Figure 4

A

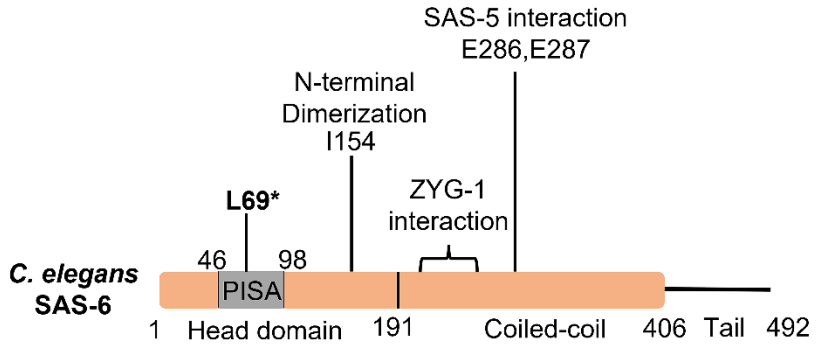

Residues involved in coiled-coil dimer interactions: L36, S58, F61, E62, L64, L172, I173, H175, L176, L177, C180, A184

Residues involved in N-terminal dimer interactions: D82, D83, T84, V85, F90, V93, T152, P153, I154, S155, K156, I159, F160

B

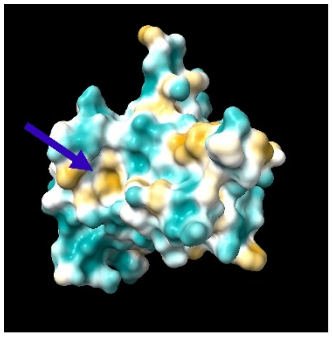

SAS-6 PDB 4G79

C

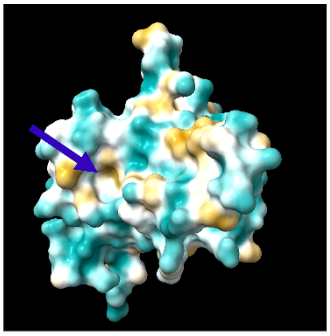

SAS-6(L69T) modeled using AlphaFold2

Figure 5

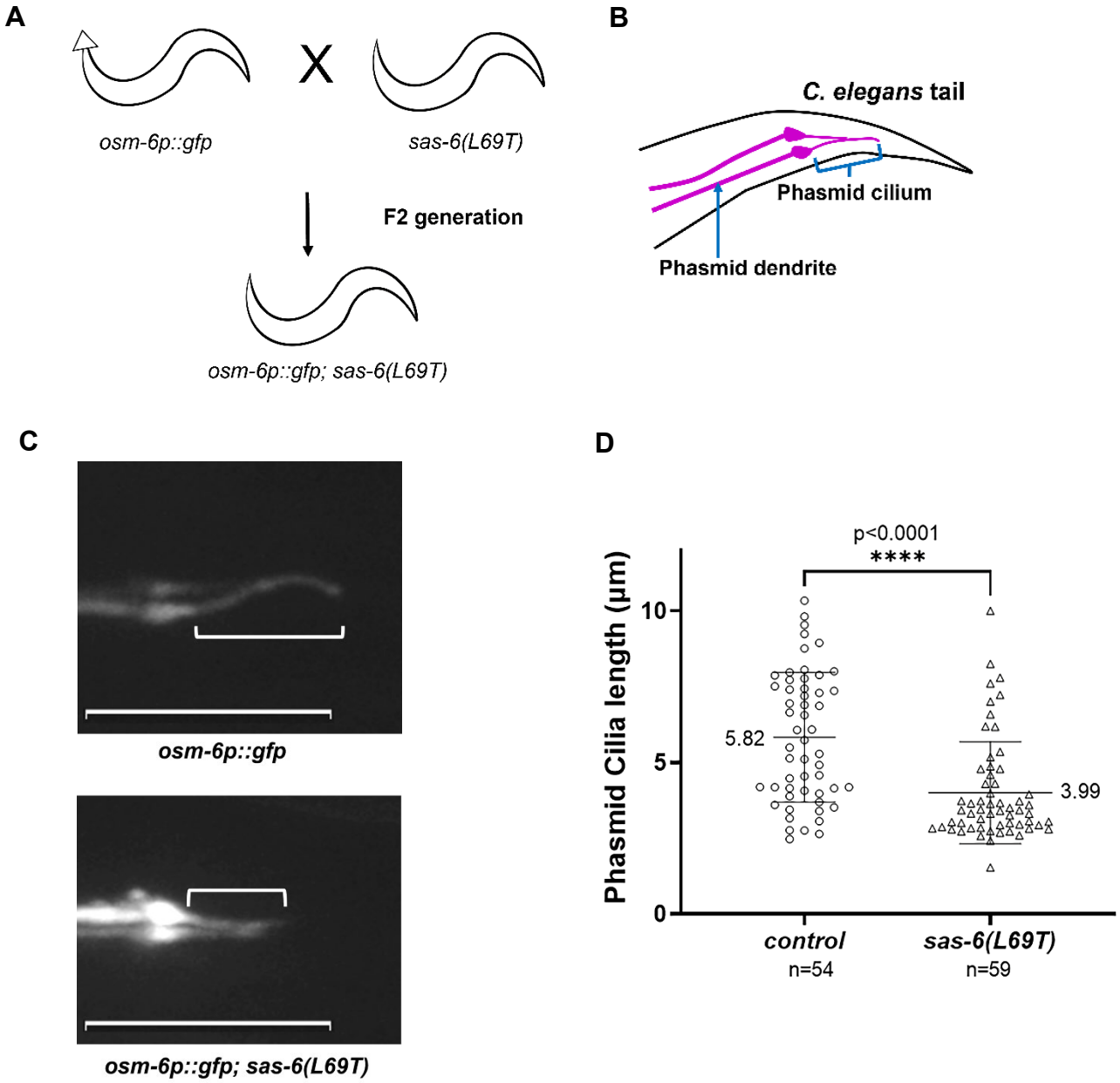
A
X
osm-6p::gfp
sas-6(L69T)
F2 generation
osm-6p::gfp; sas-6(L69T)
B
C. elegans tail
Phasmid cilium
Phasmid dendrite
C
osm-6p::gfp
osm-6p::gfp; sas-6(L69T)
D
p<0.0001
****
Phasmid Cilia length (µm)
10
5
0
5.82
3.99
control
n=54
sas-6(L69T)
n=59

Figure 6

A

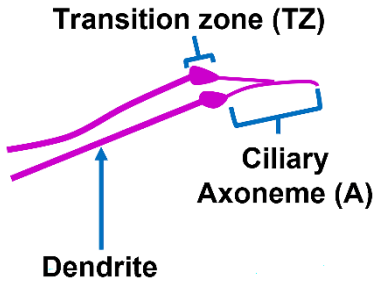

B

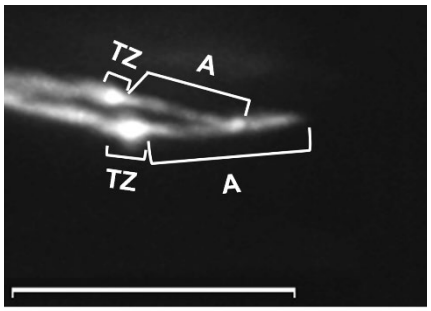

osm-6p::gfp

C

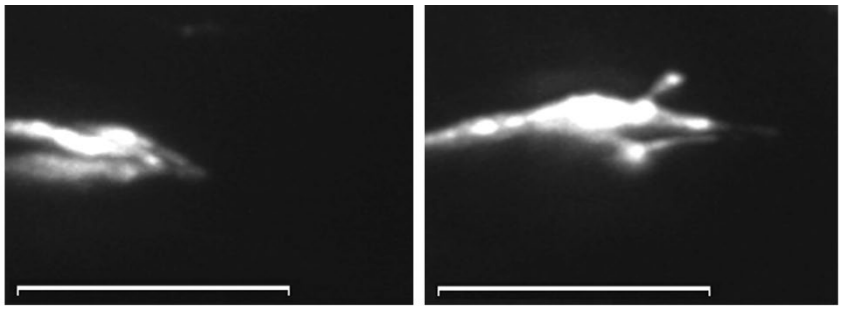

osm-6p::gfp; sas-6(L69T)

D

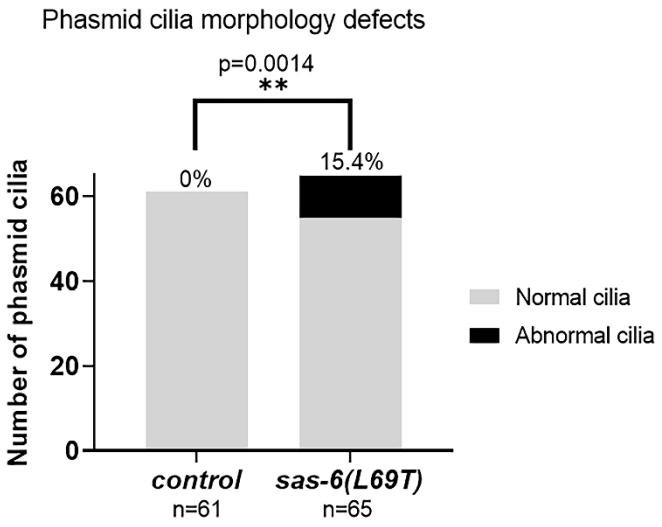

Figure 7

A

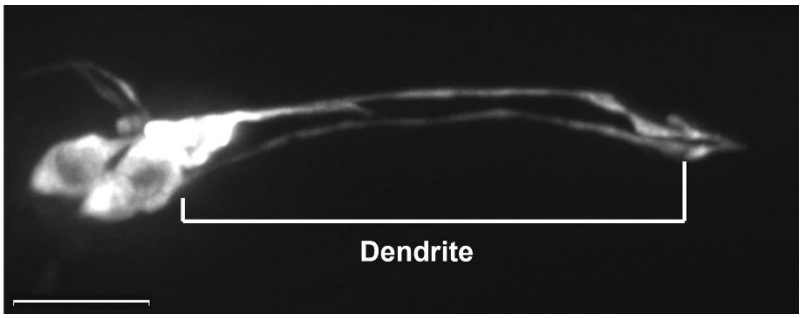
osm-6p::gfp
Dendrite

B

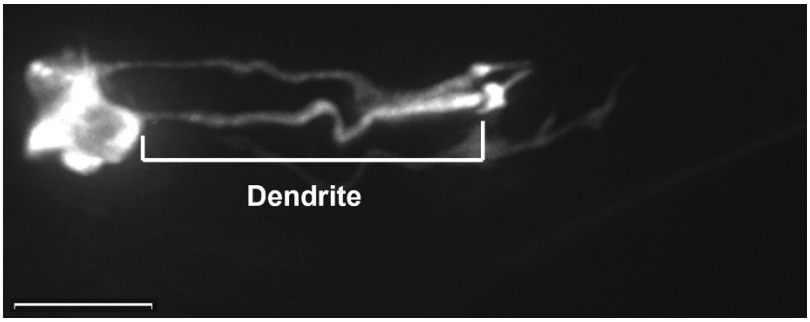
osm-6p::gfp;
sas-6(L69T)
Dendrite

C

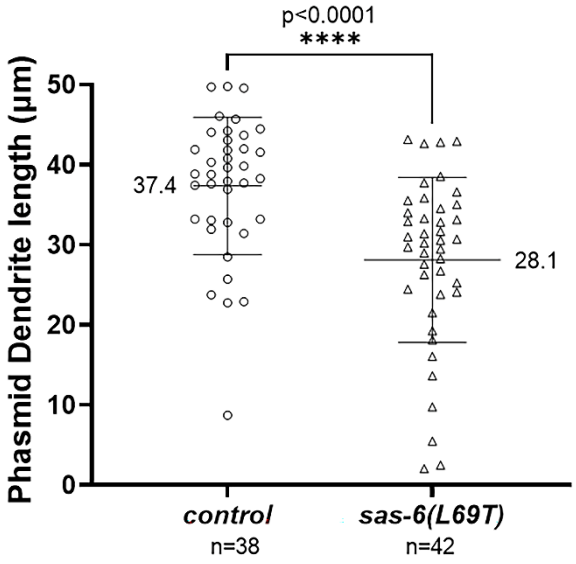
p<0.0001
****
Phasmid Dendrite length (µm)
50
40
30
20
10
0
37.4
28.1
control
n=38
sas-6(L69T)
n=42

Figure 8

A

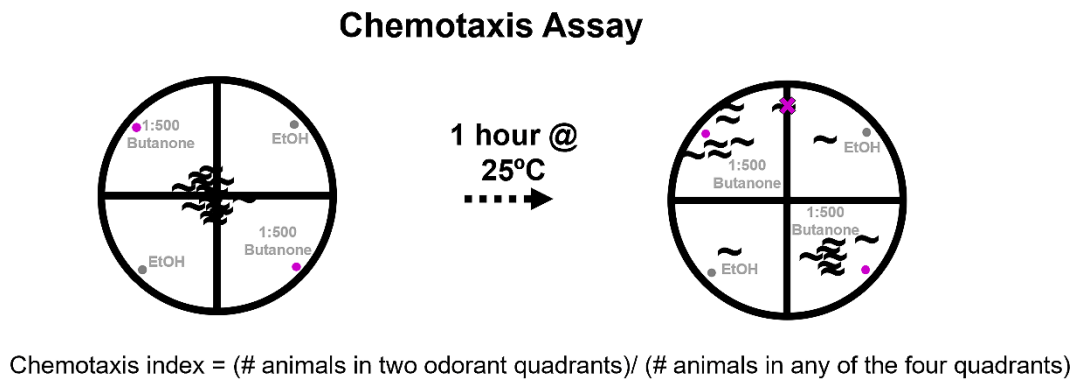

Chemotaxis index = (# animals in two odorant quadrants)/ (# animals in any of the four quadrants)

B

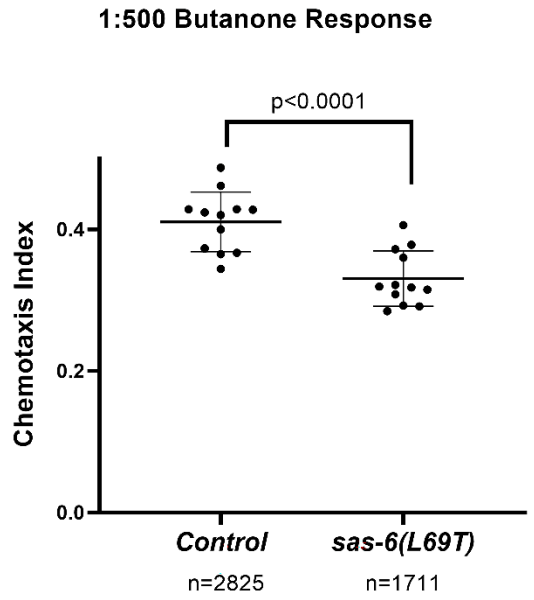

C

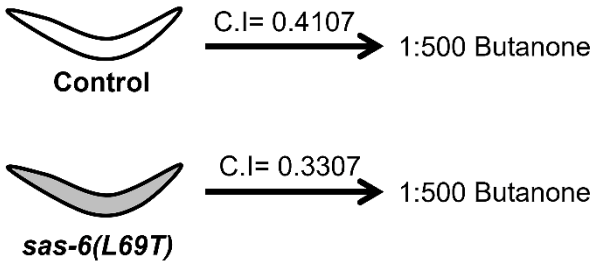

Figure S1

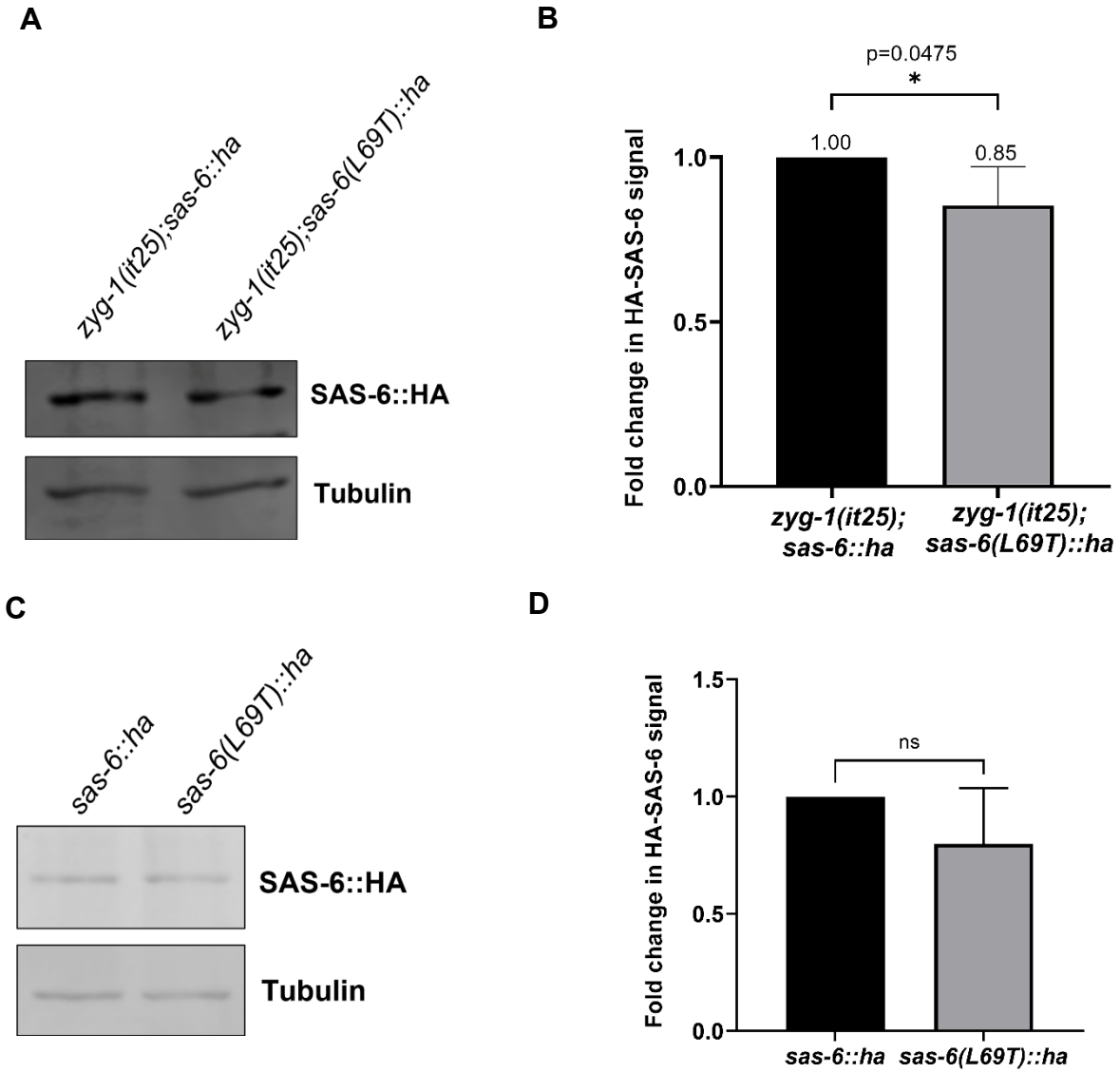
A
zyg-1(it25);sas-6::ha
zyg-1(it25);sas-6(L69T)::ha
SAS-6::HA
Tubulin
B
p=0.0475
*
1.00
0.85
Fold change in HA-SAS-6 signal
1.0
0.5
0.0
zyg-1(it25); sas-6::ha
zyg-1(it25); sas-6(L69T)::ha
C
sas-6::ha
sas-6(L69T)::ha
SAS-6::HA
Tubulin
D
ns
Fold change in HA-SAS-6 signal
1.5
1.0
0.5
0.0
sas-6::ha
sas-6(L69T)::ha